

**TRANSIENT IMPULSIVE FLOW ABOUT
A SPHERE IN A GAS STREAM**

BY

FAYEZ HASEN MOHAMMED AL-GHAMDI

MECHANICAL ENGINEERING

MARCH, 2004

**KING FAHD UNIVERSITY OF PETROLEUM & MINERALS
DHAHRAN 31262, SAUDI ARABIA**

DEANSHIP OF GRADUATE STUDIES

This thesis, written by **Fayez Hasen Mohammed Al-Ghamdi** under the direction of his thesis advisor and approved by his thesis committee, has been presented to and accepted by the Dean of Graduate Studies, in partial fulfillment of the requirements for the degree of **MASTER OF SCIENCE IN MECHANICAL ENGINEERING.**

Thesis Committee

Thesis Advisor (Dr. Mohamed A. Antar)

Thesis Co-Advisor (Dr. Maged A. I. El-Shaarawi)

Member (Dr. Syed M. Zubair)

Member (Dr. Esmail M. A. Mokheimer)

Member (Dr. Habib I. Abualhamayel)

Dr. Faleh A. Al-Sulaiman
Department Chairman

Dr. Osama A. Jannadi
Dean of Graduate Studies

Date

ACKNOWLEDGMENT

In the name of Allah, the Entirely Merciful, the Especially Merciful “Our Lord, accept [this] from us. Indeed, You are the Hearing, the Knowing.” (2:127), The Holy Quran

Acknowledgement is due to King Fahd University of Petroleum and Minerals for supporting this work and providing the required literature.

I wish to express my special appreciation to my thesis advisor, Dr. Mohammed Antar for his generous and continuous help, encouragement, suggestions and patience throughout this work. Appreciation also goes to my thesis co-advisor, Dr. Maged El-Shaarawi for his valuable guidance, suggestions and advice.

I would also like to extend my thanks to the other members of my thesis committee, Dr. Syed Zubair, Dr. Habib Abualhamayel and Dr. Esmail Mokheimer for their interest, cooperation and encouragement.

CONTENTS

	Page
ACKNOWLEDGMENT	iii
LIST OF FIGURES	viii
LIST OF TABLES	xi
ABSTRACT (English)	xii
ABSTRACT (Arabic)	xiii
NOMENCLATURE	xiv
CHAPTER I: INTRODUCTION	1
1.1 General	1
1.2 Scope of the Present Work	1
CHAPTER II: LITERATURE SURVEY	3
2.1 Introduction	3
2.2 Forced Flow Over a Solid Sphere Without Heat/Mass Transfer	3
2.2.1 Steady Flow	3
2.2.2 Unsteady Flow	4
2.3 Forced Flow Over a Solid Sphere With Heat/Mass Transfer	6
2.3.1 Steady Flow and Steady Heat Transfer	6
2.3.2 Steady Flow and Transient Heat Transfer	7
2.3.3 Unsteady Flow and Transient Heat Transfer	7
CHAPTER III: GOVERNING EQUATIONS	10
3.1 Introduction	10

3.2 Assumptions	10
3.3 Governing Equations	11
3.3.1 Governing Equations in Dimensional Form	13
3.3.2 Dimensionless Form of Equations	13
3.3.3 Boundary and Initial Conditions	14
CHAPTER IV: NUMERICAL REPRESENTATION OF THE	
GOVERNING EQUATIONS	17
4.1 Introduction	17
4.2 Numerical Grid	18
4.3 Linearizing Technique	21
4.4 Finite-Difference Representation of the Derivatives	23
4.5 Finite-Difference Representation of the Meridional Momentum Equation	24
4.6 Finite-Difference Representation of the Continuity Equation	25
4.7 Finite-Difference Representation of the Boundary and Initial Conditions	26
CHAPTER V: METHOD OF SOLUTION	28
5.1 Introduction	28
5.2 Numerical Grid	28
5.3 Criterion for Convergence	29
5.4 Flow Separation	31
5.5 Calculating Engineering Parameters	32
5.5.1 Shear Stress at the Surface of Sphere	32
5.5.2 Friction Coefficient	32
5.5.3 Drag Coefficient	32

5.5.4 Vorticity at the Surface of Sphere	33
5.6 Solution Procedure	33
5.6.1 Steady State Solution (1 st Program)	33
5.6.2 Transient Solution (2 nd Program)	34
CHAPTER VI: RESULTS AND DISCUSSION	36
6.1 Introduction	36
6.2 Meridional Velocity Profiles	36
6.3 Radial Velocity Profiles	48
CHAPTER VII: ENGINEERING PARAMETERS	56
7.1 Introduction	56
7.2 Surface Shear Stress	56
7.3 Friction Coefficient	61
7.4 Drag coefficient	61
7.5 Surface Vorticity	67
7.6 Variation of separation Angle with Time	67
7.7 Time to Reach Steady State	68
CHAPTER VIII: CONCLUSIONS AND RECOMMENDATIONS	71
8.1 Conclusions	71
8.2 Recommendations for Future Work	72
REFERENCES	73
APPENDIX A: ORDER OF MAGNITUDE ANALYSIS FOR THE	
GOVERNING EQUATIONS	76
A.1 Order of Magnitude Analysis for the Continuity Equation	76

A.2 Order of Magnitude Analysis for the Meridional Momentum Equation	77
A.3 Order of Magnitude Analysis for the Radial Momentum Equation	79

LIST OF FIGURES

	Page
Fig. 3-1: Orthogonal curvilinear coordinate system	12
Fig. 4-1: Special numerical grid for a given time	20
Fig. 4-2: Grid points involved in difference representations of the governing equations for a given time	22
Fig. 5-1: Effect of reducing grid size on the values of meridional velocity at $\theta = 60^\circ$, $Re = 5000$	30
Fig. 6-1a: Transient development of meridional velocity for $Re = 5000$, $\theta = 30^\circ$	37
Fig. 6-1b: Transient development of meridional velocity for $Re = 5000$, $\theta = 60^\circ$	37
Fig. 6-1c: Transient development of meridional velocity for $Re = 5000$, $\theta = 90^\circ$	39
Fig. 6-2a: Transient development of meridional velocity for $Re = 10,000$, $\theta = 30^\circ$	39
Fig. 6-2b: Transient development of meridional velocity for $Re = 10,000$, $\theta = 60^\circ$	40
Fig. 6-2c: Transient development of meridional velocity for $Re = 10,000$, $\theta = 90^\circ$	40
Fig. 6-3a: Meridional velocity at $\theta = 60^\circ$ for different Reynolds numbers, $t = 0.00010$	42
Fig. 6-3b: Meridional velocity at $\theta = 60^\circ$ for different Reynolds numbers, $t = 0.00040$	42
Fig. 6-3c: Meridional velocity at $\theta = 60^\circ$ for different Reynolds numbers, $t = 0.00070$	43
Fig. 6-3d: Meridional velocity at $\theta = 60^\circ$ for different Reynolds numbers at steady state	43
Fig. 6-4a: Meridional velocity for $Re = 5,000$ at different angles, $t = 0.00010$	44
Fig. 6-4b: Meridional velocity for $Re = 5,000$ at different angles, $t = 0.00040$	44
Fig. 6-4c: Meridional velocity for $Re = 5,000$ at different angles, $t = 0.00070$	45

Fig. 6-4d: Meridional velocity for $Re = 5,000$ at different angles at steady state	45
Fig. 6-5: Transient behavior of meridional velocity for $Re = 5000$ and $Z = 0.020$ at different angles	47
Fig. 6-6: Transient behavior of meridional velocity for $Re = 5000$ and $\theta = 30^\circ$ at different radial locations	47
Fig. 6-7a: Transient development of radial velocity for $Re = 5000$, $\theta = 30^\circ$	49
Fig. 6-7b: Transient development of radial velocity for $Re = 5000$, $\theta = 60^\circ$	49
Fig. 6-7c: Transient development of radial velocity for $Re = 5000$, $\theta = 90^\circ$	50
Fig. 6-8a: Transient development of radial velocity for $Re = 10,000$, $\theta = 30^\circ$	50
Fig. 6-8b: Transient development of radial velocity for $Re = 10,000$, $\theta = 60^\circ$	51
Fig. 6-8c: Transient development of radial velocity for $Re = 10,000$, $\theta = 90^\circ$	51
Fig. 6-9a: Radial velocity at $\theta = 60^\circ$ for different Reynolds numbers, $t = 0.00040$	53
Fig. 6-9b: Radial velocity at $\theta = 60^\circ$ for different Reynolds numbers, $t = 0.00070$	53
Fig. 6-9c: Radial velocity at $\theta = 60^\circ$ for different Reynolds numbers at steady state	54
Fig. 6-10a: Radial velocity for $Re = 5,000$ at different angles, $t = 0.00040$	54
Fig. 6-10b: Radial velocity for $Re = 5,000$ at different angles, $t = 0.00070$	55
Fig. 6-10c: Radial velocity for $Re = 5,000$ at different angles at steady state	55
Fig. 7-1a: Transient development of the surface shear stress for $Re = 1000$	57
Fig. 7-1b: Transient development of the surface shear stress for $Re = 5000$	57
Fig. 7-1c: Transient development of the surface shear stress for $Re = 10,000$	58
Fig. 7-2: Effect of Reynolds number on the surface shear stress at a given time ($t = 0.00040$)	60

Fig. 7-3: Transient behavior of surface shear stress for $Re = 5000$ at different angles	60
Fig. 7-4a: Transient development of friction coefficient for $Re = 1000$	63
Fig. 7-4b: Transient development of friction coefficient for $Re = 5000$	63
Fig. 7-4c: Transient development of friction coefficient for $Re = 10,000$	64
Fig. 7-5: Effect of Reynolds number on the friction coefficient at a given time ($t = 0.0004$)	64
Fig. 7-6: Transient behavior of drag coefficient at different values of Reynolds number	65
Fig. 7-7: Transient development of surface vorticity for $Re = 1000$	69
Fig. 7-8: Steady state surface vorticity compared with the boundary-layer solution of [1]	69
Fig. 7-9: Effect of Reynolds number on the variation of separation angle with time	70
Fig. 7-10: Effect of Reynolds number on the time required to reach steady state	70

LIST OF TABLES

	Page
Table 7-1: Comparison between the steady state drag coefficient of the present analysis and the results of El-Shaarawi et al. work [5]	66

THESIS ABSTRACT

Name : Fayez Hasen Mohammed Al-Ghamdi

Title : TRANSIENT IMPULSIVELY STARTED GAS FLOW ABOUT A SPHERE

Major Field : Mechanical Engineering

Date of Degree : 2003

The objective of the present work is to investigate numerically the unsteady impulsively started fluid flow about a solid sphere. A finite-difference scheme has been developed to solve the 3-D boundary-layer governing equations for a wide range of Reynolds number.

Two computer programs were developed to analyze the flow field around the sphere. The first program is used mainly to determine the boundary-layer thickness at steady state condition. The output of this program is used as an input to the second program which is developed mainly to solve the governing equations in transient conditions.

Over the studied range of Reynolds number ($1000 \leq Re \leq 10,000$), results are presented in terms of velocity components. Engineering parameters such as surface shear stress, friction coefficient and drag coefficient are also calculated and presented. Detailed transient profiles are shown for different Reynolds number and meridional angle. Comparisons with results found in the literature are carried out to validate the present analysis.

خلاصة الرسالة

الاسم	: فايز حاسن محمد الغامدي
عنوان الرسالة	: السريان المتغير مع الزمن لمائع مندفع فجأة حول كرة من الصلب
التخصص	: هندسة ميكانيكية
تاريخ الشهادة	: مارس ٢٠٠٤ م

الهدف من هذه الرسالة هو دراسة السريان المتغير مع الزمن لمائع مندفع فجأة حول كرة من الصلب باستخدام الطرق العددية. وقد تم استخدام طريقة الفروق العددية لحل المعادلات ثلاثية الأبعاد لسريان المائع في الطبقة المتاخمة لسطح الكرة وذلك على نطاق واسع لرقم رينولدز.

وقد تم تصميم برنامجين لتحليل سريان المائع حول الكرة. يقوم البرنامج الأول بتحديد سماكة الطبقة المتاخمة لسطح الكرة في حالة الثبات مع الزمن. وتستخدم نتائج هذا البرنامج كمعطيات للبرنامج الثاني الذي صمم بشكل رئيس لحل معادلات سريان المائع في حالة التغير مع الزمن.

وقد تم عرض النتائج في النطاق المدروس لرقم رينولدز (من ١٠٠٠ إلى ١٠,٠٠٠) على شكل سرعات المائع. وكذلك تم حساب وعرض بعض المتغيرات الهندسية مثل إجهاد القص ومعامل الاحتكاك ومعامل الجر. وقد مثلت هذه النتائج المتغيرة مع الزمن كدوال متغيرة مع رقم رينولدز وزاوية الدوران. وتمت مقارنة بعض نتائج الدراسة مع نتائج مناظرة من أبحاث سابقة للتأكد من دقة البرامج المستخدمة.

NOMENCLATURE

a	radius of the sphere
C_D	dimensionless drag coefficient, $\frac{D}{\frac{1}{2} \pi \rho U_\infty^2 a^2}$
C_f	local friction coefficient, $\frac{\tau_o}{\frac{1}{2} \rho U_\infty^2}$
m	number of steps of the numerical mesh network in the x-direction
n	number of steps of the numerical mesh network in the z-direction
r	radius of a circular cross section of the sphere by a plane perpendicular to the main stream direction
R	dimensionless radius of a circular cross section of the sphere by a plane perpendicular to the main stream direction, $2r/aRe$
Re	Reynolds number, $2U_\infty a/\nu$
t^*	time
t	dimensionless time, $t = \frac{\nu t^*}{a^2}$
t_{ss}	dimensionless time to reach steady state
T_x	dimensionless shear stress in the meridional direction at the surface of the sphere, $\frac{\tau \sqrt{Re/2}}{\rho U_\infty^2}$
u	meridional (x-direction) component of velocity
u^*	potential flow velocity component in the x-direction, $-(\partial\psi/\partial r)/(r \sin \theta) = U_\infty \sin \theta [1 + a^3/(2r^3)]$

- U dimensionless meridional component of velocity, u/U_∞
- U^* dimensionless potential flow velocity component in the x-direction, u^*/U_∞
- U_∞ free stream velocity
- w radial (z-direction) velocity component
- w^* radial (z-direction) velocity component of potential flow,
 $(\partial\psi/\partial\theta)/(r^2 \sin \theta) = -U_\infty \cos \theta [1 - a^3/r^3]$
- W dimensionless radial velocity component, w/ U_∞
- W^* dimensionless radial velocity component of potential flow, w^*/U_∞
- x meridional coordinate
- X dimensionless meridional distance along the surface measured from the stagnation point, $2x/ Re a$
- z distance from the sphere's surface measures along the normal to the surface in the radial direction
- Z dimensionless distance perpendicular to the surface in the radial direction, z/a

Greek Symbols:

- ρ density
- θ center angle measured from the frontal stagnation line .
- μ dynamic fluid viscosity
- ν kinematic viscosity, μ/ρ
- τ shear stress in the meridional direction at the surface of the sphere, $\mu \left. \frac{\partial u}{\partial z} \right|_0$

ψ stream function of external potential flow far away from the droplet, given by

$$\psi = 0.5 u_{\infty} r^2 \sin^2 \theta \left(1 - \frac{a^3}{r^3} \right)$$

Subscripts:

s at separation point

ss steady state

CHAPTER I

INTRODUCTION

1.1 General

The flow about a solid sphere is of importance in many engineering applications. Example of such applications are solid fuels combustion, ballistics of projectile motion, re-entry of missiles, fiber coating applications and axial flow turbo-machinery.

In the present study, transient impulsive laminar flow around a solid sphere at high Reynolds numbers ($1000 \leq Re \leq 10000$) is numerically investigated utilizing a finite-difference technique. The governing boundary-layer equations are developed, non-dimensionalized and solved.

1.2 Scope of the Present Work

In the present work, a finite-difference method has been used to analyze the flow field around a solid sphere subjected to a uniform gas stream. The model is based on the boundary-layer theory and the following assumptions:

1. Laminar, axisymmetric, unsteady flow around the solid sphere.
2. Incompressible Newtonian fluid with constant physical properties.

3. Body forces are negligible.
4. Reynolds number is large enough to apply the boundary-layer theory but not to introduce turbulence which occurs at $Re \approx 300,000$.
5. The solid sphere is initially at rest and suddenly subjected to a uniform gas stream with a constant axial velocity (U_∞).
6. The flow outside the boundary-layer is the potential flow around the sphere.

This chapter included an introduction and the scope of the present work. Chapter II presents the literature survey. Chapter III will be devoted to the problem formulation, non-dimensional form of the governing equations as well as the boundary layer simplification. In Chapter IV, the grid system and finite-difference forms of the governing equations are presented. The overall solution methodology and the method employed for calculating the engineering parameters are discussed in Chapter V. The results are presented and discussed in Chapter VI for the velocity profiles and in Chapter VII for the engineering parameters. Finally, the conclusions and recommendations are included in Chapter VIII followed by the references and an appendix.

CHAPTER II

LITERATURE SURVEY

2.1 Introduction

The literature survey for the forced flow around solid spheres can be classified into two main categories. First, forced flow over solid spheres without heat/mass transfer. This category can also be subdivided into two main cases; steady and unsteady flows. Second, forced flow over solid spheres with heat/mass transfer. This later category can also be subdivided into three main cases as follows:

1. Steady flow and steady heat transfer
2. Steady flow and transient heat transfer
3. Unsteady flow and transient heat transfer

The present survey refers to the above mentioned two categories with emphasis on the unsteady case of the first category.

2.2 Forced Flow Over a Solid Sphere Without Heat/Mass Transfer

2.2.1 Steady Flow

Considerable effort was given to the numerical modeling of steady flow around a sphere at moderate Reynolds number ($0.1 \leq Re \leq 100$) by **Jenson** [1] and **Dennis and**

Walker [2], **Hamielec et al.** [3] and **Pruppacher et al.** [4] who used different numerical methods to study the drag coefficient and vortex structure of steady flow.

In 1985, **El-Shaarawi et al** [5] investigated numerically the steady axisymmetric laminar boundary-layer flow about a rotating sphere which is subjected to a uniform stream in the direction of the axis of rotation for Reynolds number of 10,000 and for spin parameter ranging from 0 to 10,000. A finite-difference scheme was developed to solve the governing boundary-layer equations. Results were presented for the meridional and azimuthal velocities and for the wall-shear-stress components.

2.2.2 Unsteady Flow

Less attention has been given to unsteady flow problem over a sphere. **Rimon and Cheng** [6] studied numerically the transient axisymmetric flow for the uniform incompressible, homogeneous fluid flow around a sphere. Complete Navier-Stokes equations were solved for $1 \leq Re \leq 1000$ where a recirculatory wake appears. Time dependent stream function-vorticity equation in a finite-difference representation on an expanding polar grid system by Dufort-Frankel approximation for time and space was applied. They presented the detailed vorticity distribution around the sphere and values of drag coefficient which agree with standard drag curve over the investigated range of Reynolds number. They recommended curvilinear coordinates with variable mesh size as being highly desirable to obtain quantitative results and reported that downstream outflow boundary condition is of great importance.

Dennis and Walker [7] investigated numerically the transient flow past a sphere which is impulsively started from rest with constant velocity in a viscous fluid. They reported that the calculation of the flow at early times was performed using boundary-layer variables which leads to more accurate solutions. The problem was formulated in terms of stream function and vorticity. Numerical solutions were presented for cases of $Re=20, 40, 100, 200, 500, 1000$ and ∞ .

The flow around an accelerating spherical particle of diameter ranging from 50 to 200 μm in the Reynolds number range $0.1 \leq Re \leq 100$ was studied by **Li and Boulos** [8]. The flow around the sphere is assumed to be laminar and two-dimensional axisymmetric. They calculated the drag coefficient and compared it with the theoretical predictions of added mass term and Basset history term. Appropriate corrections for those two terms were proposed as functions of the acceleration rate and the particle diameter.

Unsteady axisymmetric incompressible laminar flow generated by spherical particle injected into a constant-property Newtonian fluid oscillating with time in the same direction of the particle motion was investigated by **Kim et al.** [9]. The equations governing the accelerated motion of the spherical particle were solved numerically using an axisymmetric implicit finite-difference algorithm. The results were compared with the numerical solution of the full Navier-Stokes equations for unsteady, axisymmetric flow around a freely moving sphere injected into an initially stationary or oscillating fluid. The comparison for the particle Reynolds number in the range of 2 to 150 and the particle to

fluid density ratio in the range of 5 to 200 indicates that the existing equations deviate considerably from the Navier-Stokes equations. Therefore, a new equation for the particle motion was proposed. The temporal structure of the near wake of the unsteady, axisymmetric flow around a freely moving sphere injector into initially stagnant fluid was also examined. It was found that as the sphere decelerates, the recirculation eddy size grows monotonically even though the instantaneous Reynolds number of the sphere decreases.

2.3 Forced Flow Over a Solid Sphere With Heat/Mass Transfer

2.3.1 Steady Flow and Steady Heat Transfer

In 1992, **El-Shaarawi and Al-Jamal** [10] investigated the laminar forced convection about a rotating sphere that is subjected to a uniform stream in the direction of the axis of rotation. The boundary-layer equations governing this case were solved using a finite-difference scheme for a fluid of $Pr = 0.7$ over wide range of Reynolds number and Taylor number. The traditional kinds of heating condition were considered: uniform wall temperature and uniform surface heat flux. Results at considerably large values of spin parameter (Ta/Re^2) up to 20,000 were presented for the local and average Nusselt numbers. Results show that heat transfer for air flowing past a sphere can considerably be increased by rotating it about a diameter parallel to the air stream direction.

2.3.2 Steady Flow and Transient Heat Transfer

Abramzon and Elata [11] presented a numerical study of the problem of unsteady convection from a sphere at finite Peclet numbers in a Stokesian flow field which is suddenly introduced into a fluid of different temperature. They reported that the advection of the convection process accelerates the approach of equilibrium.

Feng and Michaelides [12] obtained an asymptotic solution for the heat transfer from a sphere, which undergoes a step temperature change in a Stokesian velocity field. The solution obtained is for finite but low Peclet numbers. They found that in the case of step temperature change, the history terms are reduced to an analytical expression of the error function.

2.3.3 Unsteady Flow and Transient Heat Transfer

Michaelides and Feng [13] performed an analytical analysis analogous to those for the derivation of the equation of motion of the sphere. The temperature field was decomposed into the undisturbed field and a disturbed one where the disturbance is due to the presence of the sphere. They derived a solution to the unsteady conduction problem from a sphere at low Peclet numbers and discovered the existence of a history term, analogous to the "Basset" term in the equation of motion of a sphere.

Recently, **Feng and Michaelides** [14] extended the analytical methods used in their earlier work and obtained an analytical solution for the general problem of transient

heat transfer from a particle with arbitrary shape in a transient temperature field. The velocity field is not restricted to be Stokesian, as in most of the previous studies. Results are applied to the case of a sphere undergoing a step temperature change and a good agreement was observed with the derived expressions for the transient heat transfer from a sphere at low Peclet and asymptotic steady-state solutions.

The initial laminar thermal boundary-layer flow past an impulsively started translating and spinning rotational symmetric body of uniform temperature is investigated by **Ozturk and Ece** [15]. It was assumed that the sphere surface temperature was raised above the ambient temperature impulsively at the start of the motion. Velocity components and temperature were expanded in series in powers of time. General results were applied to a sphere. It was found that the surface heat flux is reduced in the neighborhood of the point of separation and enhanced by the reversed flow inside the separated region.

Mansoorzadeh et al. [16] developed a numerical simulation of flow past a heated/cooled sphere. A Galerkin finite element method is used to solve the 3-D incompressible Boussinesq equations in primitive variable form. The drag coefficient for adiabatic flow shows good agreement with the standard correlations over the range of the Reynolds numbers investigated ($Re = 25, 100, 400$). It is shown that the drag can vary considerably with heating of the sphere.

Then, **Takhar et al.** [17] carried out an analysis to determine the development of momentum and heat transfer occurring in the laminar boundary-layer of an incompressible viscous electrically conducting fluid in the stagnation region of rotating sphere caused by the impulsive motion of the free stream velocity and the angular velocity of the sphere. At the same time, the surface temperature is also suddenly increased. The analysis included both short and long solutions. The boundary-layer equations governing the flow were solved numerically using an implicit finite-difference scheme. It was found that the shear stresses in the longitudinal and rotating directions and the heat transfer increase with time, magnetic field, buoyancy parameter and the rotation parameter.

The conducted survey demonstrates a gap in the literature for results of unsteady flow around a sphere at high values of Reynolds number (i. e. $Re > 1000$). The present work aims at covering the still existing gap by solving the boundary-layer equations governing the unsteady impulsive flow about a solid sphere subjected to a uniform gas stream at high values of Reynolds number. A finite-difference scheme developed by **El-Shaarawi et al.** [5] has been utilized and extended here to take into consideration the unsteady term of velocities in the momentum equations. Numerical results of velocity components around the sphere at different times will be presented for a wide range of Reynolds number. Moreover, engineering parameters such as wall shear stress, drag coefficient and friction coefficient will be calculated.

CHAPTER III

GOVERNING EQUATIONS

3.1 Introduction

In this chapter, the governing equations that describe the transient impulsive flow around the solid sphere are presented. The detailed derivation of these equations starting from the Navier-Stokes equations for spherical polar coordinates, transformation of the governing equations to the orthogonal curvilinear coordinates, non-dimensionalizing, and order of magnitude analysis that is carried on to simplify the equations are found in [5] and [18].

3.2 Assumptions

The main assumptions that are employed in the derivation of the governing equations are given hereunder:

1. Laminar, axisymmetric, unsteady flow around the solid sphere.
2. Incompressible Newtonian fluid with constant physical properties.
3. Body forces are negligible.
4. Reynolds number is large enough to apply the boundary-layer theory but not to introduce turbulence.

5. The solid sphere is initially at rest and suddenly subjected to a uniform gas stream with a constant axial velocity (U_∞).
6. The flow outside the boundary-layer is the potential flow around the sphere.

3.3 Governing Equations

In this work, the orthogonal curvilinear coordinates shown in Figure (3.1) are used. The x-axis is measured along the surface of the sphere starting from the front stagnation point and extends in the meridional direction till the rear stagnation point. The z-axis passes through the sphere origin where its zero value is at the surface of the sphere. Refer to Appendix A for the detailed transformation of the governing equations from spherical polar coordinates to its orthogonal curvilinear coordinates.

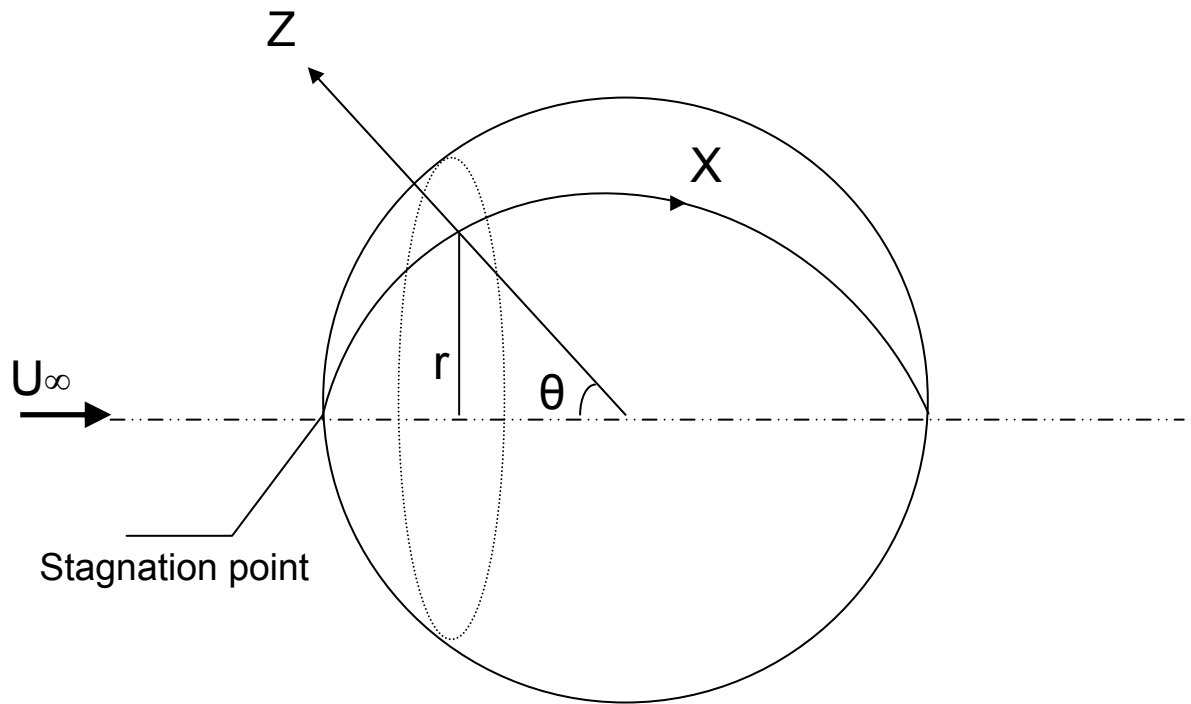


Fig. 3-1: Orthogonal curvilinear coordinate system

3.3.1 Governing Equations in Dimensional Form

Based on the assumptions mentioned in paragraph (3.2), the governing equations in the orthogonal curvilinear coordinate system are as follows: [5,18]

Continuity Equation

$$\frac{\partial w}{\partial z} + \frac{\partial u}{\partial x} + \frac{2w}{(a+z)} + \frac{u \cot \theta}{(a+z)} = 0 \quad (3.1)$$

Meridional Momentum Equation

$$\frac{\partial u}{\partial t^*} + w \frac{\partial u}{\partial z} + u \frac{\partial u}{\partial x} + \frac{uw}{(a+z)} = -\frac{1}{\rho} \frac{\partial p}{\partial x} + \nu \left[\frac{1}{(a+z)} \frac{\partial^2 [(a+z)u]}{\partial z^2} + \frac{\partial^2 u}{\partial x^2} + \frac{\cot \theta}{(a+z)} \frac{\partial u}{\partial x} + \frac{2}{(a+z)} \frac{\partial w}{\partial x} - \frac{u}{(a+z)^2 \sin^2 \theta} \right] \quad (3.2)$$

Radial Momentum Equation

$$\frac{\partial w}{\partial t^*} + w \frac{\partial w}{\partial z} + u \frac{\partial w}{\partial x} - \frac{u^2}{(a+z)} = -\frac{1}{\rho} \frac{\partial p}{\partial z} + \nu \left[\frac{1}{(a+z)} \frac{\partial^2 [(a+z)w]}{\partial z^2} + \frac{\partial^2 w}{\partial x^2} + \frac{\cot \theta}{(a+z)} \frac{\partial w}{\partial x} - \frac{2}{(a+z)} \frac{\partial u}{\partial x} - \frac{2w}{(a+z)^2} - \frac{2u \cot \theta}{(a+z)^2} \right] \quad (3.3)$$

3.3.2 Dimensionless Form of Equations

The following non-dimensionalizing parameters are used to obtain the dimensionless form of the governing equations:

$$U = \frac{u}{U_\infty} \quad W = \frac{w}{U_\infty} \quad Z = \frac{z}{a} \quad X = \frac{2x}{a \text{Re}} \quad \text{Re} = \frac{2U_\infty a}{\nu}$$

$$U^* = \frac{u^*}{U_\infty} \quad P = \frac{p}{\rho U_\infty^2} \quad t = \frac{\nu t^*}{a^2}$$

Using the above dimensionless parameters and carrying out an order of magnitude analysis, the final form of the governing boundary-layer equations becomes: [5,18]

Continuity Equation

$$\frac{\partial U}{\partial X} + \frac{\text{Re}}{2} \frac{\partial W}{\partial Z} + \text{Re} \frac{W}{(1+Z)} + \frac{\text{Re}}{2} U \frac{\text{Cot}\theta}{(1+Z)} = 0 \quad (3.4)$$

Meridional Momentum Equation

$$\frac{\partial U}{\partial t} + U \frac{\partial U}{\partial X} + \frac{\text{Re}}{2} W \frac{\partial U}{\partial Z} = U^* \frac{\partial U^*}{\partial X} + \frac{\partial^2 U}{\partial Z^2} \quad (3.5)$$

The radial momentum equation is dropped out completely since all its terms are of a lower order of magnitude. It should be noted that although the third term in the continuity equation has a lower order of magnitude than the other three terms, it was kept in the equation to take curvature effects into consideration (El-Shaarawi [19]).

3.3.3 Boundary and Initial Conditions

To determine the required number of boundary and initial conditions, it is necessary to investigate the boundary-layer equations presented in the previous section. In these equations, only the first derivative of U with respect to X is available. Therefore, only one boundary condition in the meridional direction is required. This boundary condition can be determined at the front stagnation point. The derivative of U with respect to Z is of second order, therefore, two boundary conditions in the radial direction should be specified. These two boundary conditions can be determined at two locations; at the surface of the sphere where the value of U is zero due to the no slip condition at the

sphere's surface and at the edge of the boundary-layer where the value of U can be taken equal to the value of the potential flow around a sphere.

Only the first derivative of W with respect to Z is present. Hence only a boundary condition at one location is enough and can be determined at the surface of the sphere where the value of W is zero (i. e. no suction or blowing is assumed). The initial condition is easily determined from the assumption that the solid sphere is initially at rest.

In summary, all boundary conditions required for the governing equations can be written in the following dimensional forms:

$$\begin{array}{ll}
 \text{at } x = 0, z > 0, t^* > 0 & \text{(stagnation line)} \quad u = 0, w = w^* \\
 \text{at } z = 0, x \geq 0, t^* \geq 0 & \text{(sphere surface)} \quad u = w = 0 \\
 \text{at } z \geq \delta, x > 0, t^* > 0 & u = u^*, w = w^* \\
 \text{at } t^* = 0 & u = w = 0
 \end{array} \quad \left. \vphantom{\begin{array}{l} \\ \\ \\ \end{array}} \right\} \quad (3.6)$$

Meridional as well as radial potential velocity components which are applied at the edge of the boundary-layer can be obtained from the theoretical potential flow around a stationary sphere [20]. Considering the sphere radius as “ a ”, stream function as “ ψ ” and the potential function as “ ϕ ” we have:

$$\psi = \frac{1}{2} u_{\infty} r^2 \sin^2 \theta \left(1 - \frac{a^3}{r^3} \right) \quad (3.7)$$

and

$$\phi = u_{\infty} r \cos \theta \left(1 + \frac{a^3}{2 r^3} \right) \quad (3.8)$$

Meridional and radial velocity components for the potential flow are related to the previous two equations by the following relations:

$$u^* = -\frac{1}{r} \frac{\partial \psi}{\partial \theta} = u_\infty \left(1 + \frac{a^3}{2(a+z)^3} \right) \sin \theta \quad (3.9)$$

and

$$w^* = -\frac{\partial \phi}{\partial r} = -u_\infty \left(1 - \frac{a^3}{2(a+z)^3} \right) \cos \theta \quad (3.10)$$

Using the non-dimensional parameters defined previously in equation (3.1), we get the following dimensionless form of the potential flow velocity components:

$$U^* = \left(1 + \frac{1}{2(1+Z)^3} \right) \sin \theta \quad (3.11)$$

and

$$W^* = -\left(1 - \frac{1}{(1+Z)^3} \right) \cos \theta \quad (3.12)$$

Similarly, the final form of the non-dimensional boundary conditions can be written as;

$$\left. \begin{array}{ll} \text{at } X=0, Z \geq 0, t > 0 & U=0, W=W^* = -\left(1 - \frac{1}{(1+Z)^3} \right) \cos \theta \\ \text{at } Z=0, X \geq 0, t \geq 0 & U=W=0 \\ \text{at } Z \geq \delta, X > 0, t > 0 & U=U^* = \left(1 + \frac{1}{2(1+Z)^3} \right) \sin \theta \\ & W=W^* = -\left(1 - \frac{1}{(1+Z)^3} \right) \cos \theta \\ \text{at } t=0 & U=W=0 \end{array} \right\} \quad (3.13)$$

Now, having the governing equations in the final dimensionless forms as well as the dimensionless boundary conditions makes the problem well posed and amenable to the numerical solution.

CHAPTER IV

NEMERICAL REPRESENTATION OF THE GOVERNING EQUATIONS

4.1 Introduction

The governing equations developed in the previous chapter are nonlinear second order equations. Since there is no analytical solution for this type of equations, approximate methods of solution are used to solve them. The method used in this work is the finite-difference approximation. In this method the governing equations are first transformed to difference equations by superimposing on the domain of solution a grid of points in the form of a mesh and the derivatives are expressed along each mesh point (referred to as a node). Therefore, the differential governing equations can be written for a set of nodes of the grid converting them to algebraic equations that are linearized to a system of linear algebraic equations and then solved by an appropriate technique for matrix inversion. In this chapter, the finite-difference representation of the governing equations as well as their boundary and initial conditions are presented [18].

4.2 Numerical Grid

Figure (4.1) shows the numerical grid which is used to solve the governing equations for a given value of time. The grid consists of two sets of perpendicular lines which represent the meridional direction (circles) and the radial direction (straight lines). The intersections of these lines constitute the spacial mesh points (nodes) where the solutions of the governing equations are obtained for a given value of time. The circles are concentric and start from the surface of the sphere with constant Z values and extended until the edge of the boundary-layer. The straight lines pass through the center of the sphere and each of them is a constant X -line (at a constant angle).

The spacial grid consists of $(n + 1)$ points in the radial direction where the first being on the sphere ($Z = 0$) and the last is located outside the boundary-layer edge. On the other hand, the grid has $(m + 1)$ meridional stations starting from $X=0$ (at the front stagnation line) and extending until the angle of flow separation. The index i represents the radial value of the mesh points (Z -direction) starting with $i = 1$ at the surface of the sphere ($Z = 0$) till $i = n + 1$ in the free stream while the index j represents the meridional value of the mesh points (X -direction) starting from $j = 1$ at the front stagnation line ($X = 0$) till the point of separation where $j = m + 1$. Similarly, the index k represents the value of the dimensionless time (t), starting with $k=1$ for $t = \Delta t$. Therefore, the finite-difference representation of the special mesh points will be as follows:

$$Z_i = (i - 1) \Delta Z \quad \text{where } i = 1, 2, 3, \dots, n + 1$$

$$X_j = (j - 1) \Delta X \quad \text{where } j = 1, 2, 3, \dots, m + 1$$

Here, ΔX and ΔZ represent the step sizes of the meridional and the radial directions, respectively, and the subscripts denote the location of the variable under consideration, e.g. $U_{i,j,k}$ means the meridional velocity at the i 'th radial location and j 'th meridional direction at the k 'th time interval .

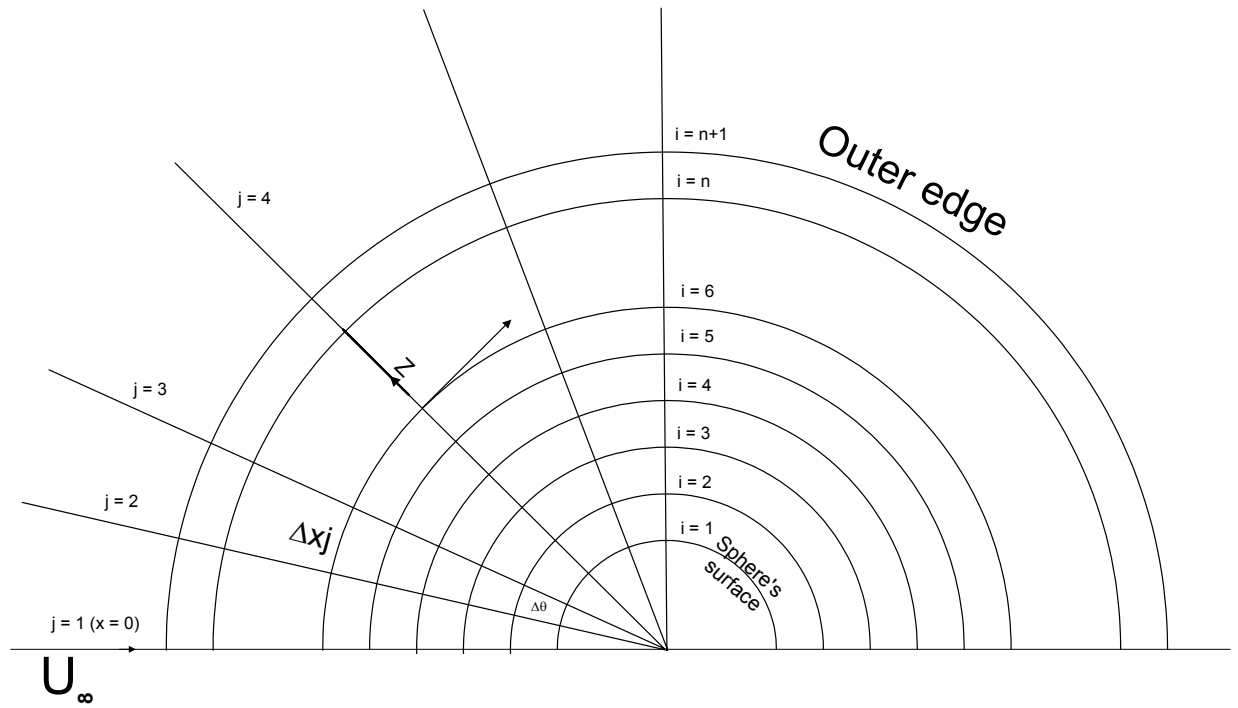


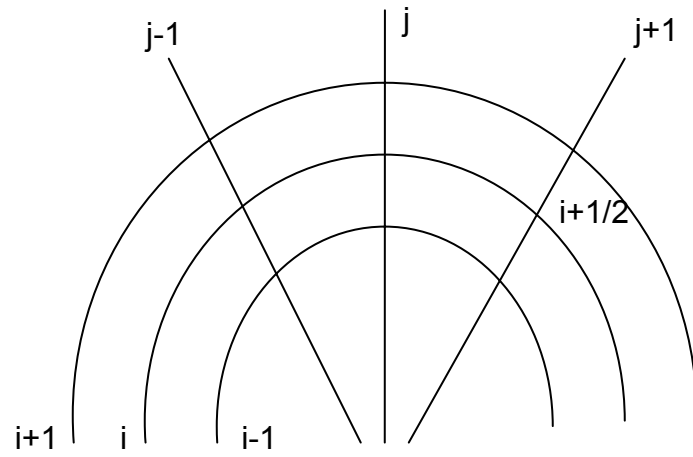
Fig. 4-1: Spacial numerical grid for a given time

4.3 Linearizing Technique

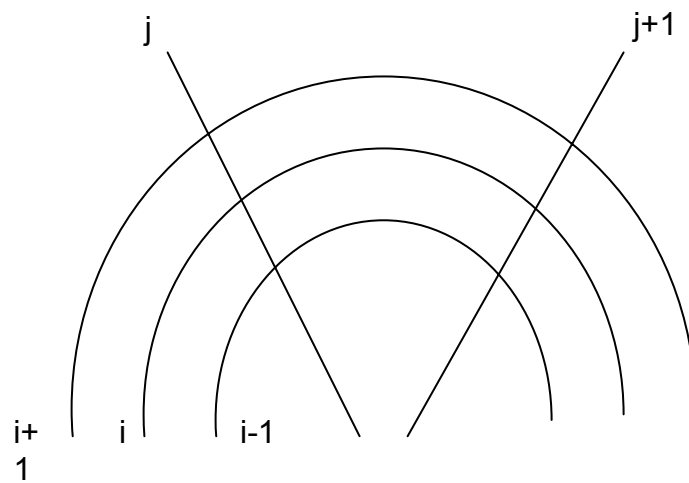
The finite-difference formulation of the governing equations should retain the same characteristics of the parent equations developed in the previous chapter. The governing boundary-layer equations are parabolic in nature with the terms in the marching direction (X) are the convective terms while those in the transverse (Z) are diffusive. Therefore, backward differences are utilized for the convective terms and central differences are utilized for the diffusive terms.

For each meridional location, the variables with subscript (j) will be assumed to be known and those with subscripts ($j + 1$) are assumed to be unknown for all values of (i). The solution for all (i) variables will be organized in a matrix form solved along the constant (j) lines then it marches forward for the next meridional step till the separation occurs at which the solution stops for the current time step and restarts from the beginning for the next time step. The whole solution will terminate when the steady state condition of flow is reached.

The governing equations are approximated by finite-differences in separate domains [21] where the location of each derivative was chosen to ensure stability and consistency of solution. Following the technique used in [21] a ringed point will represent the location where derivatives are calculated while the cross points represent the grid points involved in the finite-difference approximation. For the ringed points that do not coincide on the grid points, derivatives are approximated and an average value is taken [18]. The grid points involved in the difference representations of the governing equations are shown in Figure (4.2).



Continuity equation



Meridional momentum equation

Fig. 4-2: Grid points involved in difference representations of the governing equations for a given time.

The order by which the numerical solution is obtained starts by solving the meridional momentum equation for $U_{i,j+1,k+1}$, then the continuity equation has to be solved for $W_{i,j+1,k+1}$. Therefore, the term W found in the meridional momentum equation will be represented by $W_{i,j,k+1}$ (i. e. from the previous meridional step), while in the continuity equation U will be expressed as $U_{i,j+1,k+1}$ since it would have been already obtained from the solution of the preceding momentum equation. Then the whole procedure is repeated for the next time step until the steady state condition of flow is reached.

4.4 Finite-Difference Representation of the Derivatives

Following the notation described in the previous section and that shown in figure (4.2), the finite-difference representation of the various derivatives present in the governing equations can be written as follows:

$$\frac{\partial U}{\partial X} = \frac{U_{i,j+1,k+1} - U_{i,j,k+1}}{\Delta X_i} \quad (4.1)$$

$$\frac{\partial U}{\partial Z} = \frac{U_{i+1,j+1,k+1} - U_{i-1,j+1,k+1}}{2\Delta Z} \quad (4.2)$$

$$\frac{\partial^2 U}{\partial Z^2} = \frac{U_{i+1,j+1,k+1} - 2U_{i,j+1,k+1} + U_{i-1,j+1,k+1}}{\Delta Z^2} \quad (4.3)$$

$$\frac{\partial W}{\partial Z} = \frac{W_{i+1,j+1,k+1} - W_{i,j+1,k+1}}{\Delta Z} \quad (4.4)$$

$$\frac{\partial U}{\partial t} = \frac{U_{i,j+1,k+1} - U_{i,j+1,k}}{\Delta t} \quad (4.5)$$

4.5 Finite-Difference Representation of the Meridional Momentum Equation

$$\frac{\partial U}{\partial t} + U \frac{\partial U}{\partial X} + \frac{\text{Re } W}{2} \frac{\partial U}{\partial Z} = U^* \frac{\partial U^*}{\partial X} + \frac{\partial^2 U}{\partial Z^2} \quad (3.5)$$

$$\begin{aligned} \frac{U_{i,j+1,k+1} - U_{i,j+1,k}}{\Delta t} + U_{i,j,k+1} \frac{U_{i,j+1,k+1} - U_{i,j,k+1}}{\Delta X_i} + \frac{\text{Re } W_{i,j,k+1}}{2} \frac{U_{i+1,j+1,k+1} - U_{i-1,j+1,k+1}}{2\Delta Z} = \\ \frac{3}{2} \sin(j.\Delta\theta) \cdot \frac{3}{4} \text{Re } \cos(j.\Delta\theta) + \frac{U_{i+1,j+1,k+1} - 2U_{i,j+1,k+1} + U_{i-1,j+1,k+1}}{\Delta Z^2} \end{aligned} \quad (4.6)$$

Rearranging equation (4.6):

$$\begin{aligned} U_{i-1,j+1,k+1} \left(\frac{-W_{i,j,k+1} \text{Re}}{4\Delta Z} - \frac{1}{(\Delta Z)^2} \right) + U_{i,j+1,k+1} \left(\frac{1}{\Delta t} + \frac{U_{i,j,k+1}}{\Delta X_i} + \frac{2}{(\Delta Z)^2} \right) \\ + U_{i+1,j+1,k+1} \left(\frac{W_{i,j,k+1} \text{Re}}{4\Delta Z} - \frac{1}{(\Delta Z)^2} \right) = \frac{U_{i,j+1,k}}{\Delta t} + \frac{(U_{i,j,k+1})^2}{\Delta X_i} + \frac{9}{8} \text{Re } \sin(j.\Delta\theta) \cdot \cos(j.\Delta\theta) \end{aligned} \quad (4.7)$$

Note that $\frac{9}{8} \text{Re } \sin(j.\Delta\theta) \cdot \cos(j.\Delta\theta) = \frac{9}{16} \text{Re } \sin(2j.\Delta\theta)$

Let; $C(i) = \left(\frac{-W_{i,j,k+1} \text{Re}}{4\Delta Z} - \frac{1}{(\Delta Z)^2} \right)$ (4.8)

$$A(i) = \left(\frac{1}{\Delta t} + \frac{U_{i,j,k+1}}{\Delta X_i} + \frac{2}{(\Delta Z)^2} \right) \quad (4.9)$$

$$B(i) = \left(\frac{W_{i,j,k+1} \text{Re}}{4\Delta Z} - \frac{1}{(\Delta Z)^2} \right) \quad (4.10)$$

$$D(i) = \frac{U_{i,j+1,k}}{\Delta t} + \frac{(U_{i,j,k+1})^2}{\Delta X_i} + \frac{9}{16} \text{Re } \sin(2j.\Delta\theta) \quad (4.11)$$

$$\begin{aligned} & \frac{U_{i+1,j+1,k+1} + U_{i,j+1,k+1} - U_{i+1,j,k+1} - U_{i,j,k+1}}{2\Delta X_{i+1/2}} + \frac{\operatorname{Re} W_{i+1,j+1,k+1} - W_{i,j+1,k+1}}{2\Delta Z} + \\ & \frac{\operatorname{Re} (W_{i+1,j+1,k+1} + W_{i,j+1,k+1})}{2(1+Z_{i+1/2})} + \frac{(U_{i+1,j+1,k+1} + U_{i,j+1,k+1})\operatorname{Re} \cot(j\Delta\theta)}{4(1+Z_{i+1/2})} = 0 \end{aligned} \quad (4.15)$$

Rearranging:

$$\begin{aligned} & W_{i,j+1,k+1} \frac{\operatorname{Re} \left(\frac{1}{1+Z_{i+1/2}} - \frac{1}{\Delta Z} \right)}{2} + W_{i+1,j+1,k+1} \frac{\operatorname{Re} \left(\frac{1}{1+Z_{i+1/2}} + \frac{1}{\Delta Z} \right)}{2} = \\ & - \frac{U_{i+1,j+1,k+1} + U_{i,j+1,k+1} - U_{i+1,j,k+1} - U_{i,j,k+1}}{2\Delta X_{i+1/2}} - \frac{(U_{i+1,j+1,k+1} + U_{i,j+1,k+1})\operatorname{Re} \cot(j\Delta\theta)}{4(1+Z_{i+1/2})} \end{aligned} \quad (4.16)$$

$$\text{Let; } A(i) = \left(\frac{1}{1+Z_{i+1/2}} - \frac{1}{\Delta Z} \right)$$

$$B(i) = \left(\frac{1}{1+Z_{i+1/2}} + \frac{1}{\Delta Z} \right) \quad (4.17)$$

$$D(i) = - \frac{U_{i+1,j+1,k+1} + U_{i,j+1,k+1} - U_{i+1,j,k+1} - U_{i,j,k+1}}{2\Delta X_{i+1/2}} - \frac{(U_{i+1,j+1,k+1} + U_{i,j+1,k+1})\operatorname{Re} \cot(j\Delta\theta)}{4(1+Z_{i+1/2})}$$

Equations can be represented, for a given j, as:

$$\text{for } i = 1 : \quad A_1 W_1 + B_1 W_2 = D_1 \quad (W_1 = 0 \text{ “sphere surface”})$$

$$\text{for } i = 2 : \quad A_2 W_2 + B_2 W_3 = D_2 \quad (4.18)$$

$$\text{for } i = n-1 : \quad A_{n-1} W_{n-1} + B_{n-1} W_n = D_{n-1}$$

$$\text{for } i = n : \quad A_n W_n + B_n W_{n+1} = D_n$$

4.7 Finite-Difference Representation of the Boundary and Initial Conditions

The finite-difference form of the boundary conditions is as follows:

$$\text{at } j = 1, i \geq 1 \text{ and } k > 1 \quad U_{i,1,k} = 0 \quad (4.19-a)$$

$$W_{i,1,k} = -1 + \frac{1}{(1 + (i-1)\Delta Z)^3} \quad (4.19-b)$$

at $i = 1, j \geq 1$ and $k > 1$ $U_{1,j,k} = W_{1,j,k} = 0$ (4.19-c)

at $i = n+1, j > 1$ and $k > 1$ $U_{n+1,j,k} = \left(1 + \frac{1}{2(1+n\Delta Z)^3}\right) \sin[(j-1)\Delta\theta]$ (4.19-d)

at $t = 0$ ($k = 1$) $U_{i,j,1} = W_{i,j,1} = 0$ (4.19-e)

CHAPTER V

METHOD OF SOLUTION

5.1 Introduction

The purpose of this chapter is to show, in details, the method of solution for the problem under study. This method will be eventually used in the computer programs to generate the solution of the problem at the specified boundary and initial conditions.

Engineering parameters such as the shear stress at the surface of the sphere, the flow separation angle and the drag coefficient were also calculated during the solution and their values were presented for a wide range of Reynolds number.

5.2 Numerical Grid

The numerical grid parameters were selected to be variable and have small values in the meridional direction especially at the points where high gradients are expected as in the case of the flow near the separation point. Along each meridional station, the grid size is assumed constant ($\Delta Z = 0.001$) where a minimum number of mesh points was assumed ($n = 20$). The convergence criterion, which will be explained in the next section, was checked at the outermost point ($n+1$). If the convergence criterion was met, the solution proceeds to the next meridional step, otherwise the number of steps is increased by two

and the solution is repeated for the same meridional station until the criterion is met. The solution proceeds in the marching X-direction with an equal grid size (1°) until the point of separation is reached then the program adjusts itself and returns one meridional step back to reduce the X-direction grid size to (0.1°) in order to accurately determine the point of flow separation [18].

Grid independence test was conducted to verify the effect of reducing the grid size on the study results. It was found that further reduction in the grid size will result in an insignificant change on the obtained values. Figure 5.1 shows the effect of reducing the grid size on the values of meridional velocity at $\theta = 60^\circ$ and $Re = 5000$.

5.3 Criterion for Convergence

For the flow around a solid sphere, a minimum number of mesh points in the Z-direction for a certain meridional step was assumed to be 20. Upon calculating the meridional velocity component along this line, the tangent of the velocity at the uppermost point was calculated and the slope of the velocity ($\partial U/\partial Z$) is calculated at the uppermost point ($n + 1$). Then the slope of the potential flow around the sphere is calculated at the same point and the two values are compared. If both slopes are matched within a certain arbitrary specified tolerance (a value of 0.005 was chosen in the present work), the solution is supposed to be convergent and this would determine the edge of the boundary-layer. Otherwise, the number of the radial steps (n) is increased by two and the procedure is repeated until the matching criterion is met [18].

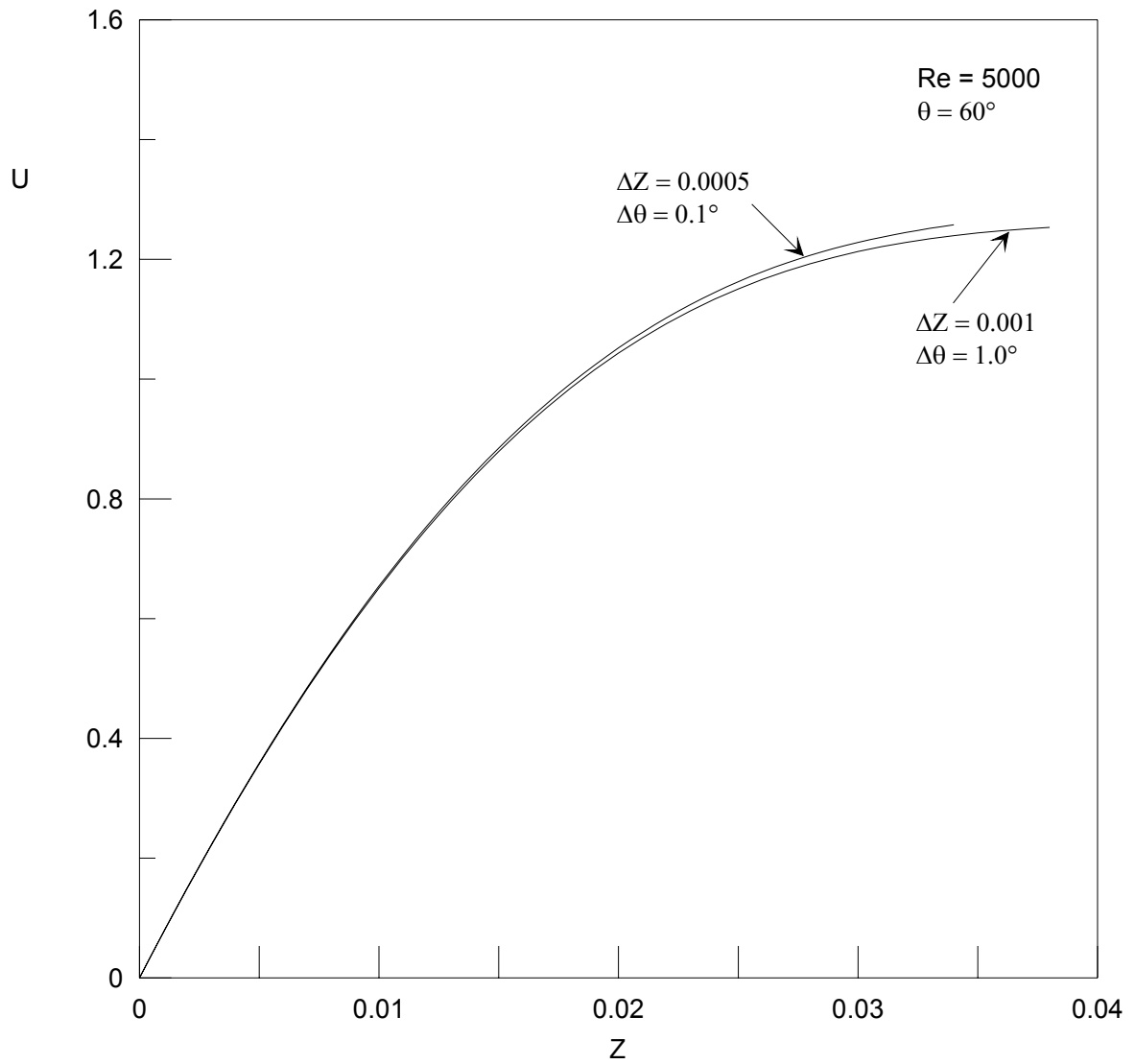


Fig. 5-1: Effect of reducing grid size on the values of meridional velocity at $\theta = 60^\circ$,
 $Re = 5000$

5.4 Flow Separation

External fluid particles accelerate in the region $0 \leq \theta \leq 90$ and decelerate in the region where $\theta > 90$, hence the pressure decreases in the accelerated region and then increases in the decelerated region [20]. Since the external pressure is suddenly imposed at the boundary-layer, the transformation of the pressure into kinetic energy takes place in the accelerated region and a great amount of the kinetic energy of the fluid particles adjacent to the wall is consumed in moving against the friction forces. In the decelerated region, the remaining kinetic energy is too small to keep these particles moving in the region of the high pressure, so, they would be eventually arrested and the external high pressure would force them to move in the opposite direction detaching from the surface of the sphere and the point of flow separation can be detected by the condition of zero velocity gradient at the wall ($\partial U / \partial Z = 0$). Therefore, the flow separation would be accompanied by the following:

1. a vanishing velocity gradient
2. a larger boundary-layer thickness due to the increase of the number of the radial steps required to satisfy the matching criterion at the edge of the boundary-layer, and
3. a larger value of the radial velocity component due to the increase of the outward flow direction.

The program is developed such that a constant meridional step is followed in the marching X-direction until the flow separation occurs where zero or negative

(unexpected) values of U can be obtained. Then a finer mesh is used in X -direction (i.e. for ΔX) and the point of separation is obtained [18].

5.5 Calculating Engineering Parameters

Upon computing the velocity field for the whole domain of numerical solution, the following engineering parameters can be calculated.

5.5.1 Shear stress at the Surface of Sphere

$$\text{Shear stress can be calculated as } \tau = -\mu \left. \frac{\partial u}{\partial z} \right|_{z=0} \quad (5.1)$$

$$\text{Or, in dimensionless form } T_x = \frac{\tau \sqrt{\text{Re}/2}}{\rho U_\infty^2} \quad (5.2)$$

$$\text{Eqn. (5.2) can be written as } T_x = \sqrt{\frac{2}{\text{Re}}} \left. \frac{\partial U}{\partial Z} \right|_{Z=0} \quad (5.3)$$

5.5.2 Friction Coefficient

$$C_f = \frac{\tau}{\frac{1}{2} \rho U_\infty^2} \quad (5.4)$$

$$\text{or } C_f = \frac{T_x}{\sqrt{\text{Re}/8}} \quad (5.5)$$

5.5.3 Drag Coefficient

$$C_D = 4 \int_0^\theta \left. \frac{\partial U}{\partial Z} \right|_{Z=0} R \sin \theta \, d\theta \quad (5.6)$$

5.5.4 Vorticity at the Surface of Sphere

$$\zeta' = \frac{u}{r} + \frac{\partial u}{\partial r} - \frac{1}{r} \frac{\partial W}{\partial \theta} \quad (5.7)$$

$$\text{or, in dimensionless form} \quad \zeta = \frac{\zeta'}{(U_{\infty}/a)} = \frac{U}{1+Z} + \frac{\partial U}{\partial Z} - \frac{2}{\text{Re}} + \frac{\partial W}{\partial X} \quad (5.8)$$

The finite-difference representation will be:

$$\zeta = \frac{U_{i,j+1}}{1+(i-1)Z} + \frac{-U_{3,j+1} + 4U_{2,j+1} - 3U_{1,j+1}}{2\Delta Z} - \frac{2}{\text{Re}} + \frac{W_{i,j+1} - W_{i,j}}{\Delta X_i} \quad (5.9)$$

5.6 Solution Procedure

Two programs were developed to solve the governing finite- difference equations obtained in Chapter IV. The first program is used only to determine the boundary-layer thickness assuming steady state conditions of flow. The output of this program is used as an input to the second program which is mainly used to solve the governing equations in transient conditions. The numerical solution is obtained by first selecting values of Reynolds number which is the main controlling parameter of these equations. The selected Reynolds number is fixed each time the two programs run. Then the solution proceeds as follows;

5.6.1 Steady-State Solution (1st Program):

1. The program starts in the marching X-direction; the variables in the first meridional station $j = 1$ (front stagnation line) are known where the boundary-layer thickness is assumed to be zero ($U = 0$ and W is obtained from the potential

flow distribution). So, the program starts to obtain solutions at the second meridional station ($j = 2$) assuming a number of radial grid points of 20.

2. The finite-difference equation representing the meridional momentum equation is solved first using Thomas algorithm. The obtained values of U are then used to solve the finite-difference equations representing the continuity equation to calculate the values of W .
3. The convergence criterion at the uppermost point is checked. If the criterion is not met, the number of radial steps (n) is increased by two and the solution is repeated again.
4. Steps 2 & 3 are repeated until the convergence criterion is met. Then the obtained values for U & W are reported and prepared to be the initial values for the next meridional step.
5. The final value of n is saved in a separate data file to be used in the second program as described in the next section.
6. The solution then proceeds in the marching X -direction repeating the previous steps (2 through 5) until the separation point is reached.

5.6.2 Transient Solution (2nd Program)

1. The program starts in the marching X -direction; the variables in the first meridional station $j = 1$ (front stagnation line) are known where the boundary-layer thickness is assumed to be zero ($U = 0$ and W is obtained from the potential flow distribution). The initial values of U and W are assumed to be zero throughout the boundary-layer. So, the program starts to obtain solutions at the

second meridional station ($j = 2$) utilizing the value of n obtained from the first program.

2. The finite-difference equations representing the meridional momentum equation is solved first using Thomas algorithm. The obtained values of U are then used to solve the finite-difference equations representing the continuity equation to calculate the values of W .
3. The obtained values for U & W are stored and prepared to be the initial values for the next meridional step.
4. The solution then proceeds in the marching X -direction repeating the previous steps (2 & 3) until the separation point is reached.
5. Engineering parameters such as the shear stress at the sphere surface, drag coefficient and friction coefficient are calculated
6. The whole solution is then advanced and repeated for the next time step until the steady state condition of flow is reached when there is no change in the values of meridional velocity at ($\theta = 105$) for two consecutive time steps.

CHAPTER VI

RESULTS AND DISCUSSION

6.1 Introduction

In this chapter, the meridional velocity profiles as well as the radial velocity profiles are presented. These profiles are plotted at different times, for different Reynolds numbers and at different meridional angles to show the effect of these parameters on the flow characteristics.

6.2 Meridional Velocity Profiles

Figures 6-1a, 6-1b and 6-1c show the transient development of the meridional velocity component U for $Re = 5000$. They are plotted at three different meridional stations (angles) measured from the front stagnation point ($\theta = 30^\circ$, $\theta = 60^\circ$ and $\theta = 90^\circ$). Initially (at $t = 0$), the meridional velocity is zero throughout the boundary-layer. As the time elapses ($t > 0$), momentum diffusion starts at the boundary-layer edge and spreads until it reaches the surface of the sphere. The gradual increase in the values of U continues until the steady state condition of flow is reached.

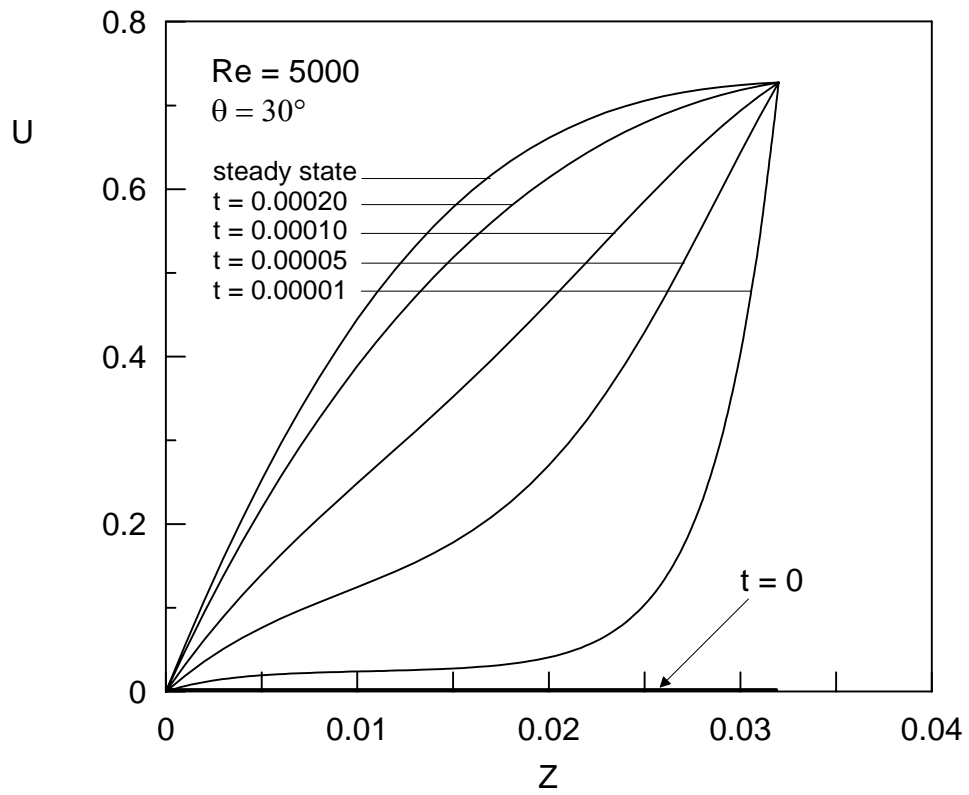


Fig. 6-1a: Transient development of meridional velocity for $Re = 5000$, $\theta = 30^\circ$

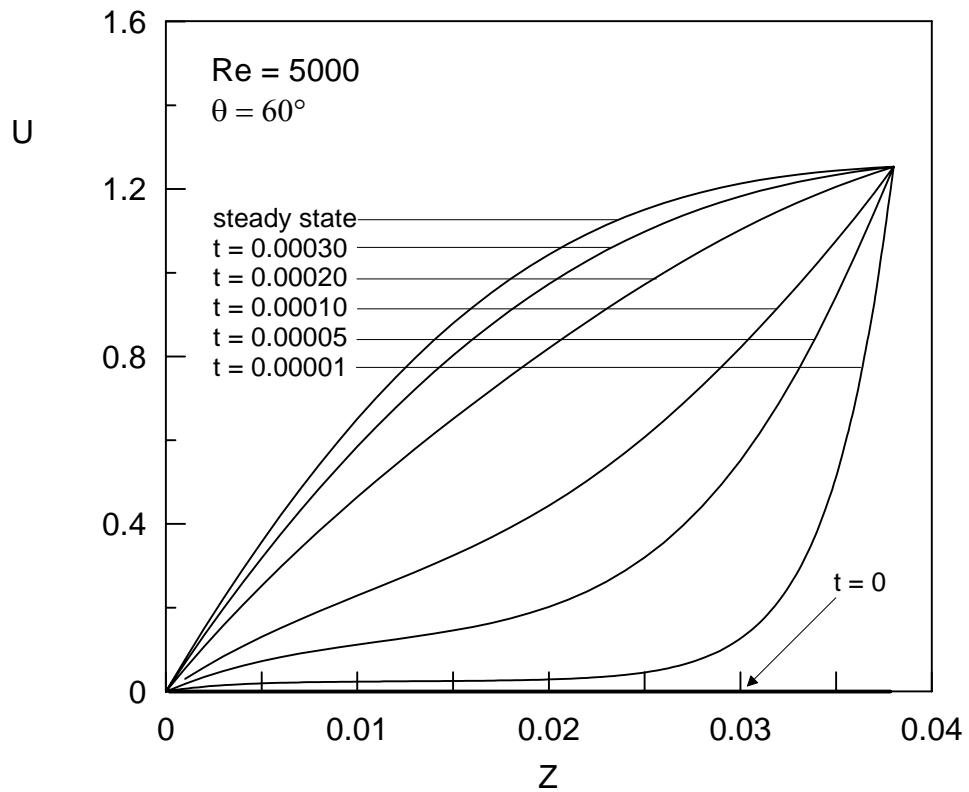


Fig. 6-1b: Transient development of meridional velocity for $Re = 5000$, $\theta = 60^\circ$

The same plots are repeated for another Reynolds number ($Re = 10,000$) as shown in Figures 6-2a, 6-2b and 6-2c and the same trend is also shown in these figures. It is worth noting that the boundary layer thickness in this case is less compared to its corresponding values for lower values of Reynolds number. This is due to the thinning effect to the hydrodynamic boundary layer at high Reynolds number due to higher velocity gradients within the boundary layer; whereas lower values of Reynolds number result in less velocity gradients within the boundary layer requiring thicker boundary layer. This notice will be emphasized in the subsequent figures. A comparison between the meridional velocity profile at $\theta = 60^\circ$ and $Re = 10,000$ of the present work and the corresponding profile for the steady state work of El-Shaarawi et al. [5] at $(Ta/Re^2) = 0$ shows that both profiles lay at the top of each other.

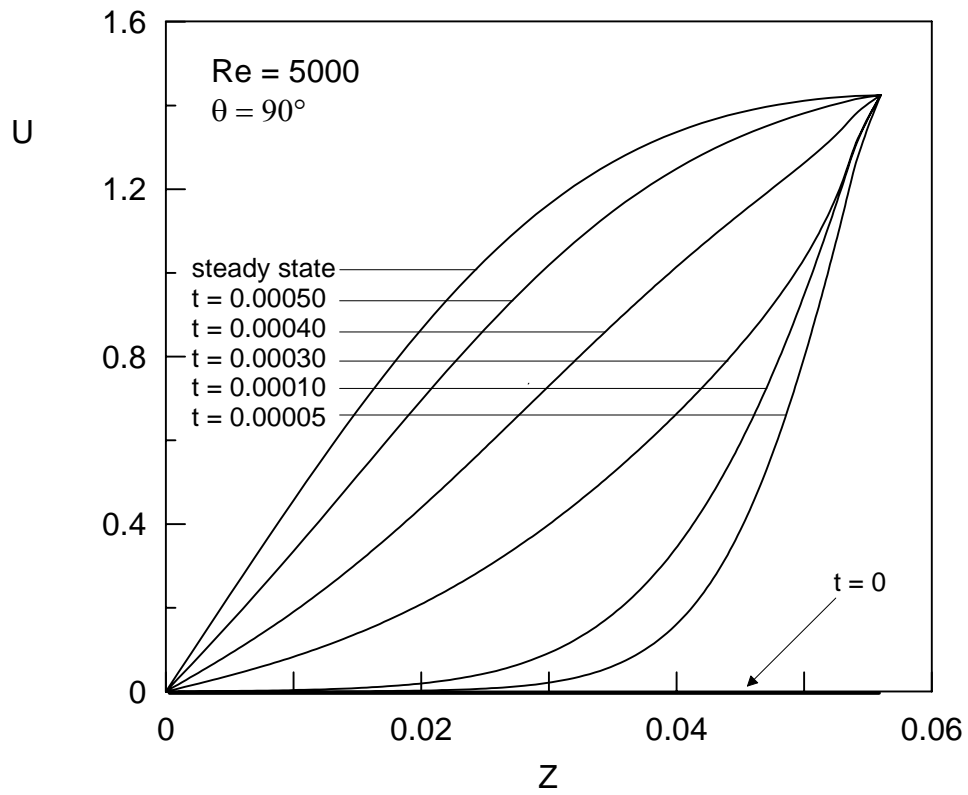


Fig. 6-1c: Transient development of meridional velocity for $Re = 5000$, $\theta = 90^\circ$

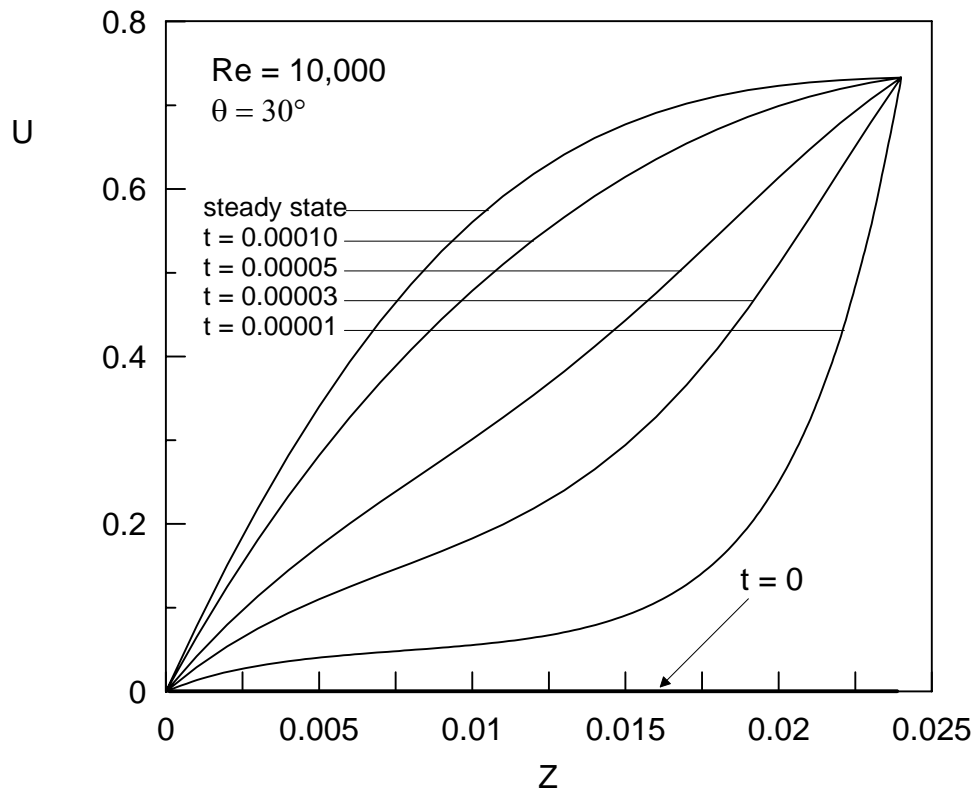


Fig. 6-2a: Transient development of meridional velocity for $Re = 10,000$, $\theta = 30^\circ$

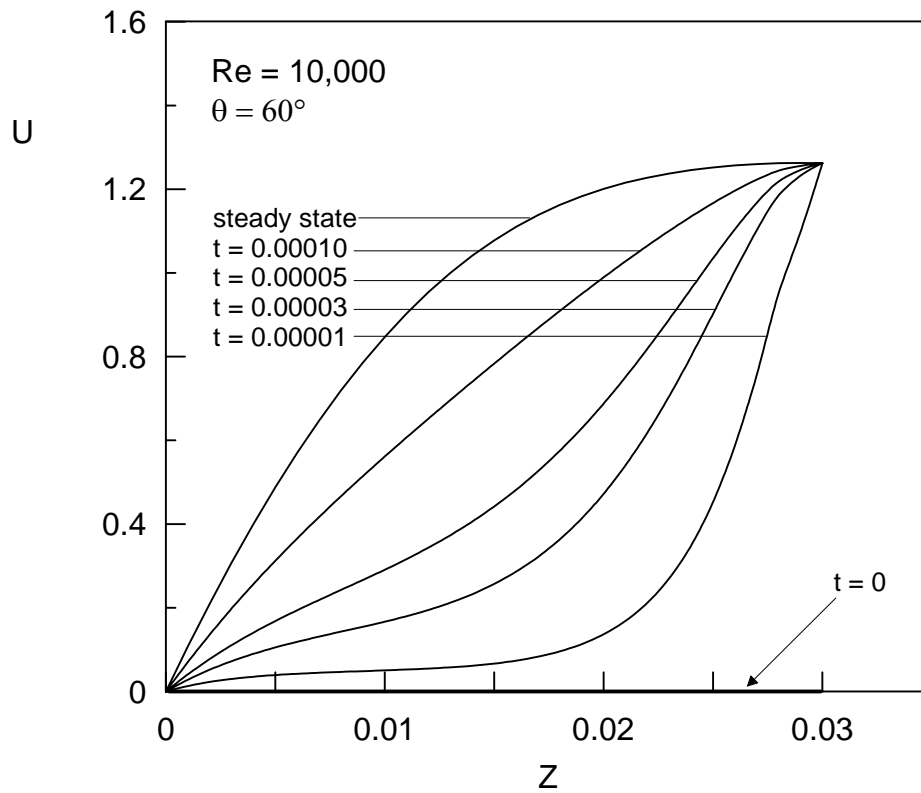


Fig. 6-2b: Transient development of meridional velocity for $Re = 10,000$, $\theta = 60^\circ$

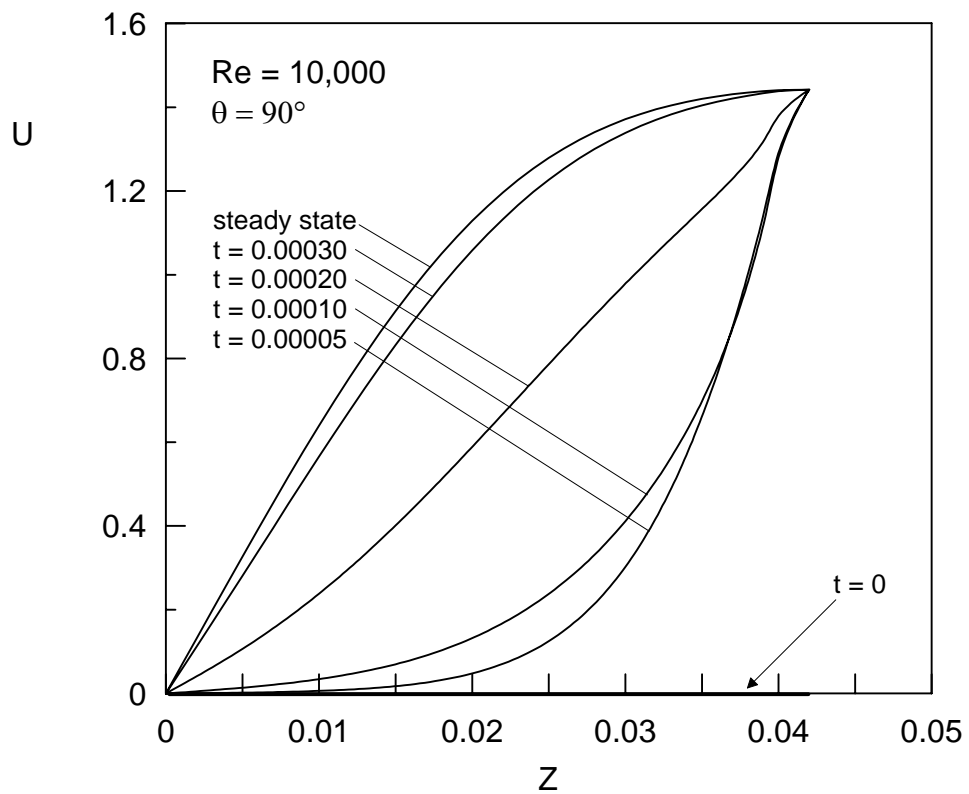


Fig. 6-2c: Transient development of meridional velocity for $Re = 10,000$, $\theta = 90^\circ$

The effect of Reynolds number on the boundary layer thickness is also shown in Figure 6-3a for $t = 0.00010$ and at certain meridional angle ($\theta = 60^\circ$). Three different values of Reynolds number $Re = 1000$, $Re = 5000$ and $R = 10,000$ are selected where it is noticed that as the Reynolds number increases, the boundary-layer thickness decreases and vice versa. As indicated earlier, this is due to the high velocity gradient, within the boundary-layer, at higher Reynolds number which requires less boundary-layer thickness for the velocity to increase from its value at the sphere surface to the free stream value. The same trend is also observed at different times, $t = 0.00040$, $t = 0.00070$ and steady state condition in Figures 6-3b, 6-3c and 6-3d, respectively.

The boundary layer development as the meridional angle increases is shown in Figures 6-4a, 6-4b, 6-4c and 6-4d at given values of time ($t = 0.00010$, $t = 0.00040$, $t = 0.00070$ and steady state). Values of meridional velocity U are plotted for a fixed value of Reynolds number ($Re = 5000$) and at three meridional angles ($\theta = 30^\circ$, $\theta = 60^\circ$ and $\theta = 90^\circ$). It is clear from the figures that the boundary-layer thickness increases from its zero value at the front stagnation point until it reaches its maximum value at the point of flow separation. This is due to the increased momentum transfer in the radial direction as the angle increases.

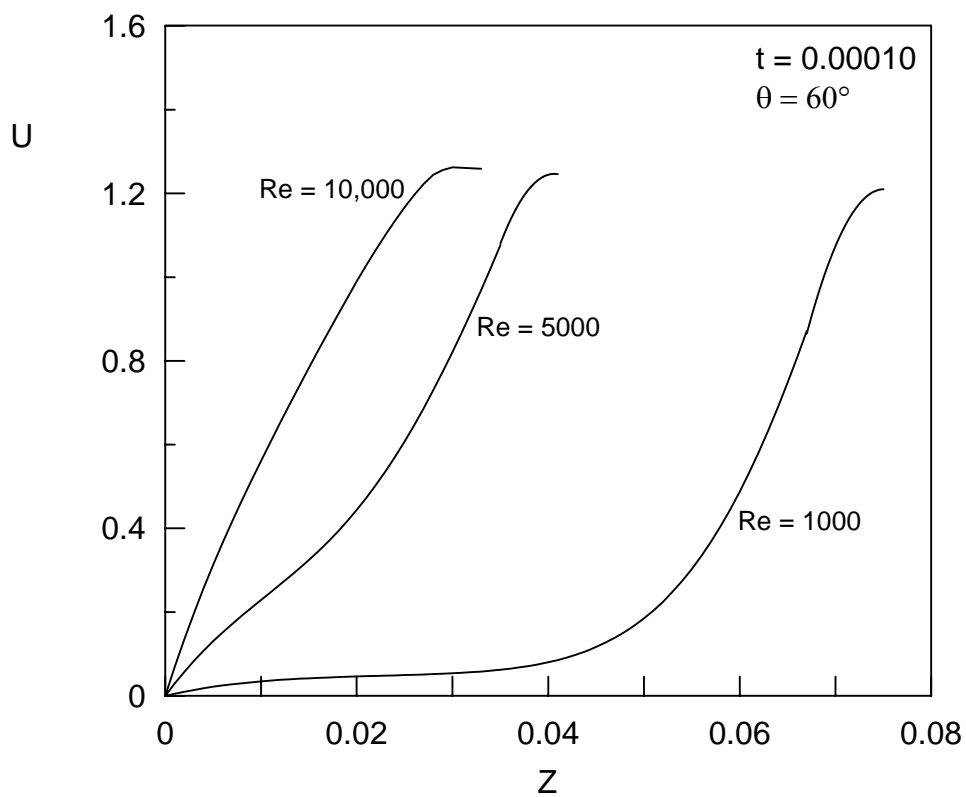


Fig. 6-3a: Meridional velocity at $\theta = 60^\circ$ for different Reynolds numbers, $t = 0.00010$

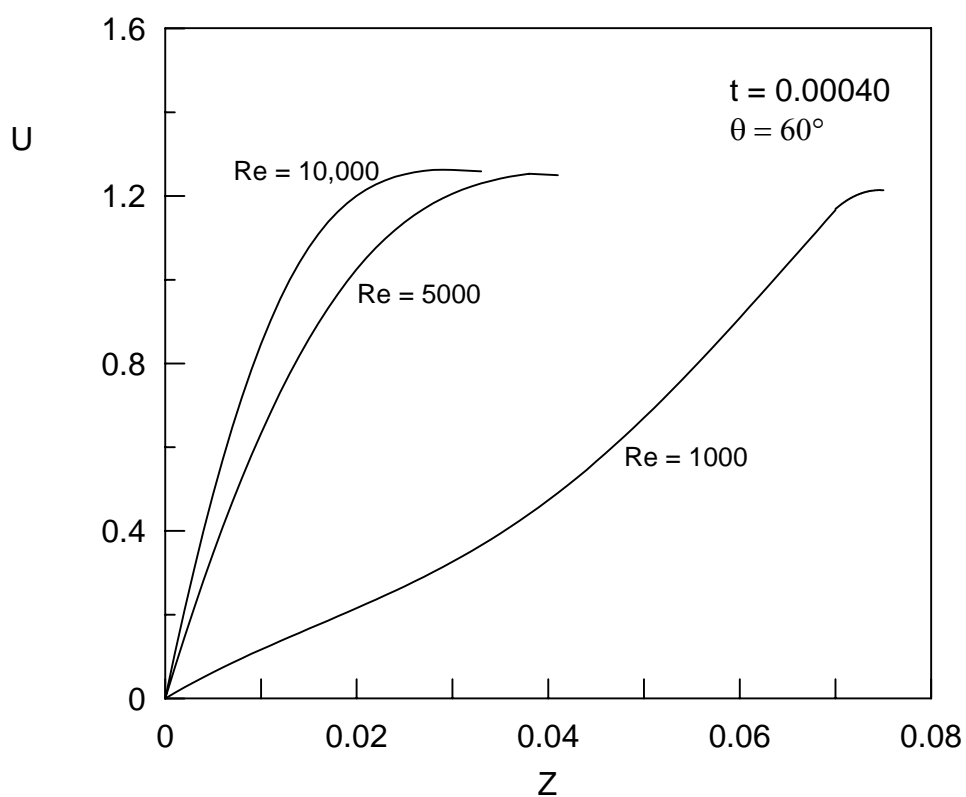


Fig. 6-3b: Meridional velocity at $\theta = 60^\circ$ for different Reynolds numbers, $t = 0.00040$

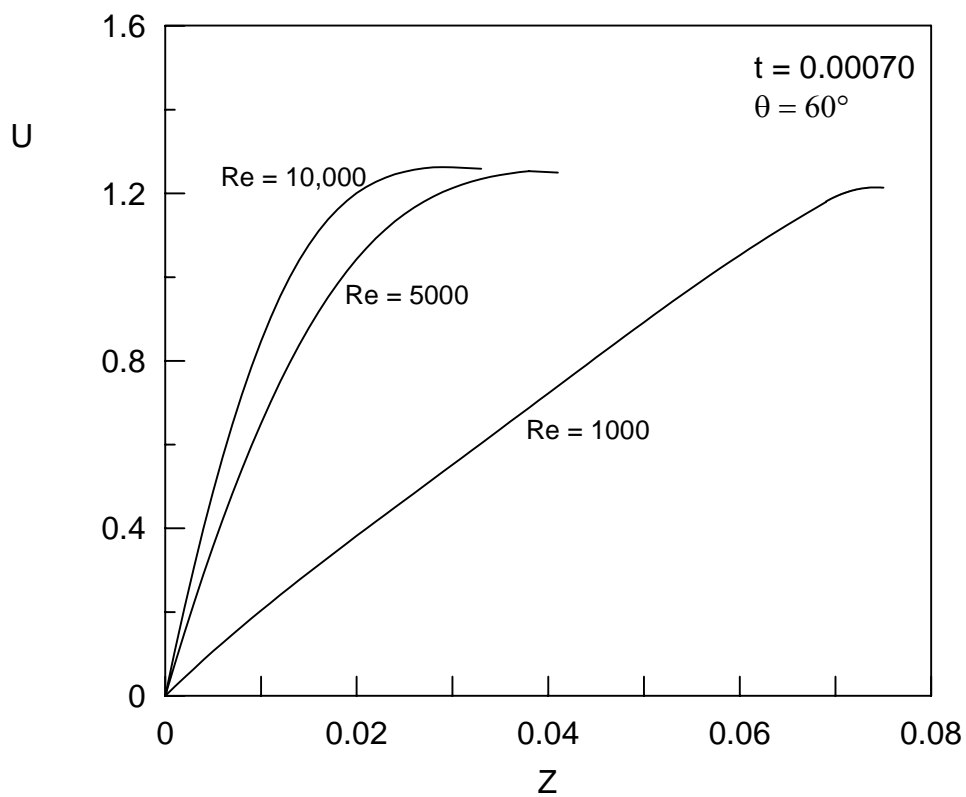


Fig. 6-3c: Meridional velocity at $\theta = 60^\circ$ for different Reynolds numbers, $t = 0.00070$

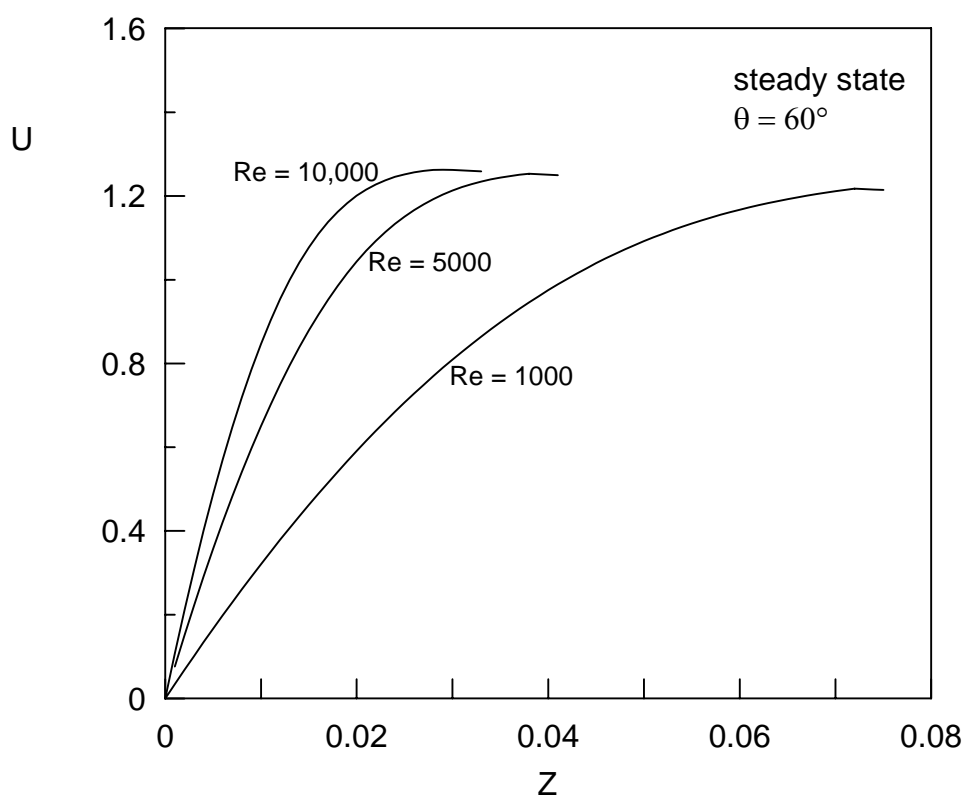


Fig. 6-3d: Meridional velocity at $\theta = 60^\circ$ for different Reynolds numbers at steady state

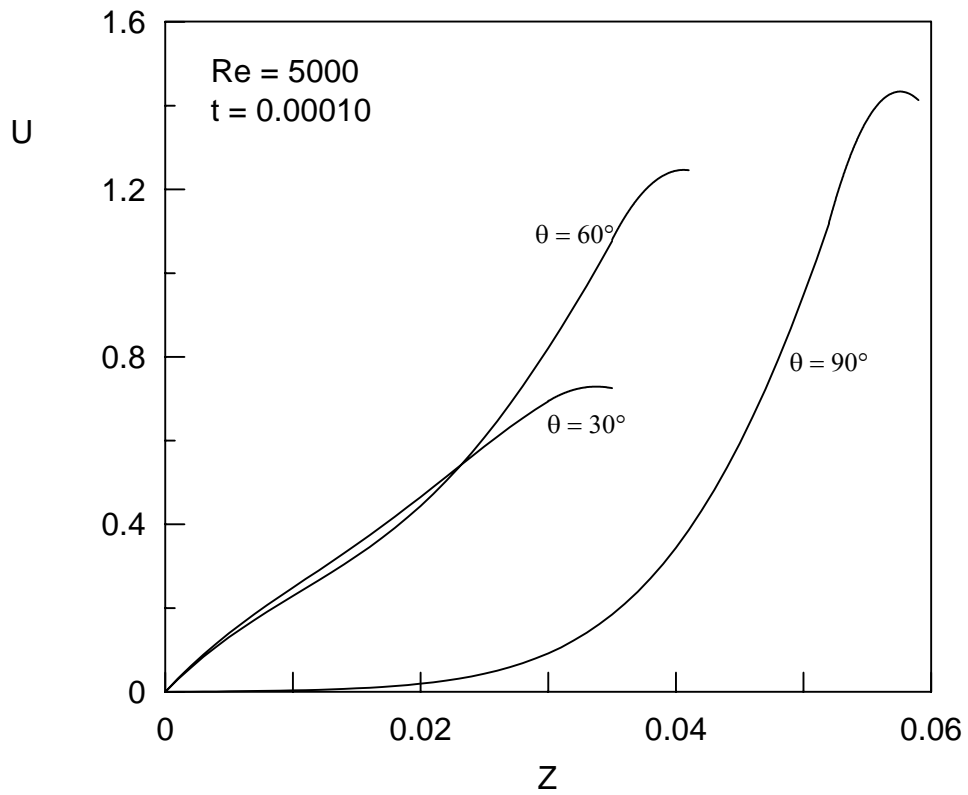


Fig. 6-4a: Meridional velocity for $Re = 5,000$ at different angles, $t = 0.00010$

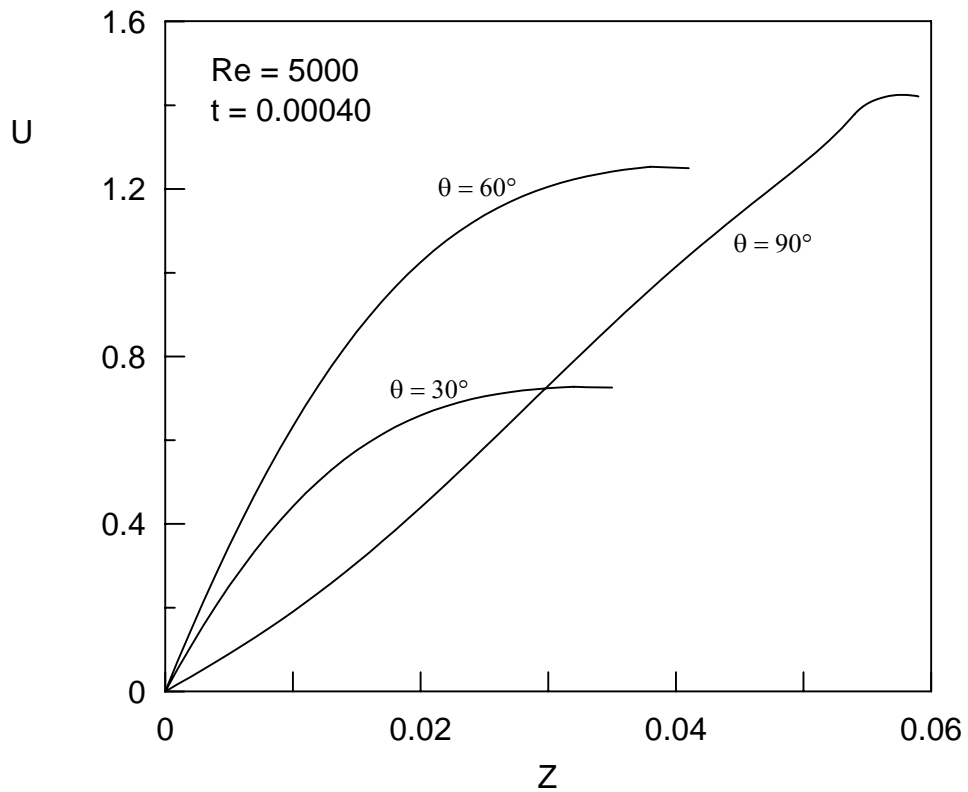
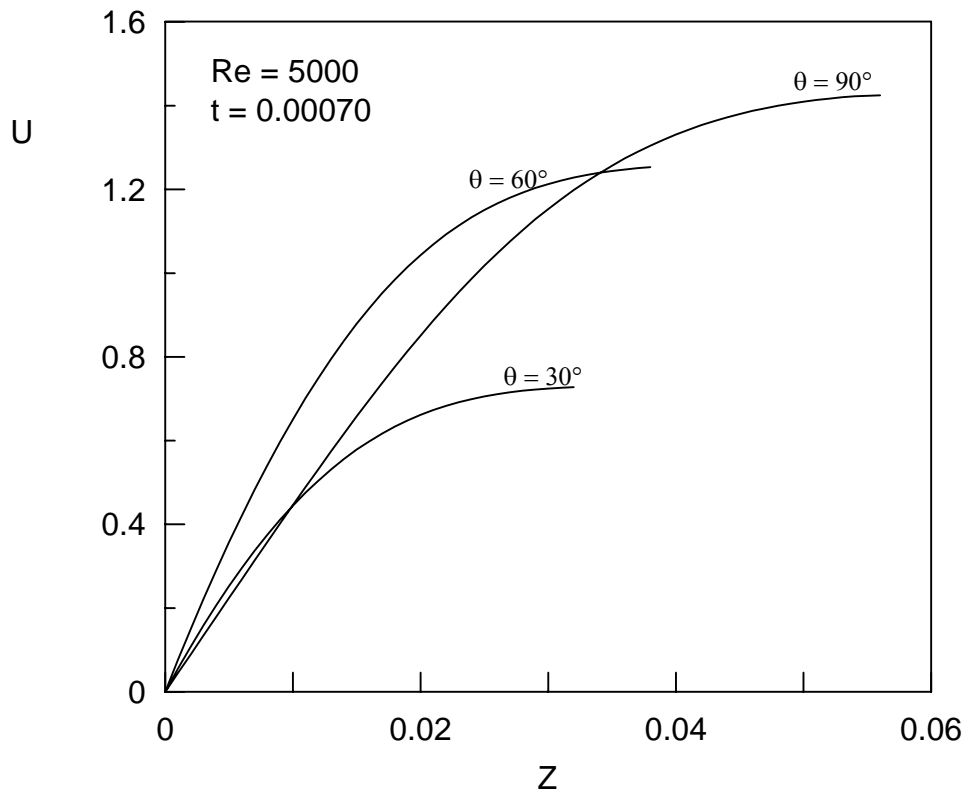
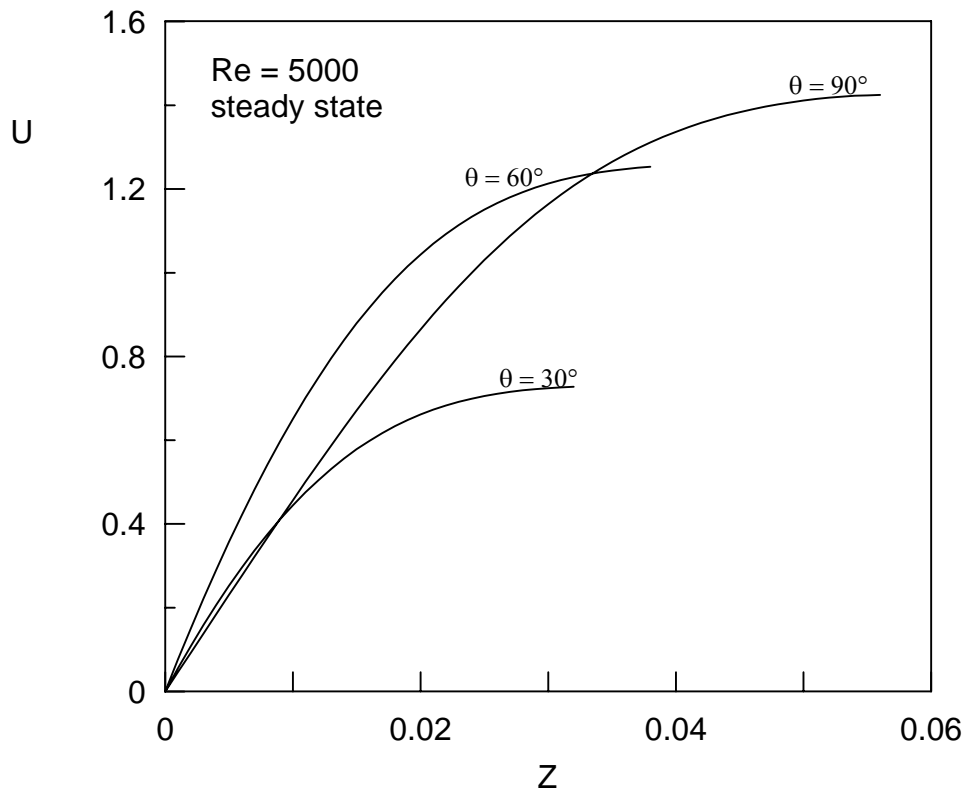


Fig. 6-4b: Meridional velocity for $Re = 5,000$ at different angles, $t = 0.00040$

Fig. 6-4c: Meridional velocity for $Re = 5,000$ at different angles, $t = 0.00070$ Fig. 6-4d: Meridional velocity for $Re = 5,000$ at different angles at steady state

The transient behavior of the meridional velocity for $Re = 5000$ and at a given value of radial location ($Z = 0.020$) is shown in Figure 6.5. Values of meridional velocity are plotted at various meridional angles. It is clear from the figure that as the time elapses ($t > 0$), the meridional velocities increase until the steady state condition of flow is reached. The figure also shows that as the meridional angle increases, the meridional velocities increase up to $\theta = 60^\circ$ then decrease. Therefore, as the meridional angle approaches the separation point, the steady state values of the meridional velocity start decreasing.

The transient behavior of the meridional velocity for $Re = 5000$ and $\theta = 30^\circ$ plotted at different radial locations is shown in Figure 6.6. As the time elapses, the meridional velocities increase until the steady state condition of flow is reached. The figure also shows that the meridional velocity values increase when moving away from the surface of the sphere. This is due to the increased momentum transfer in the radial direction.

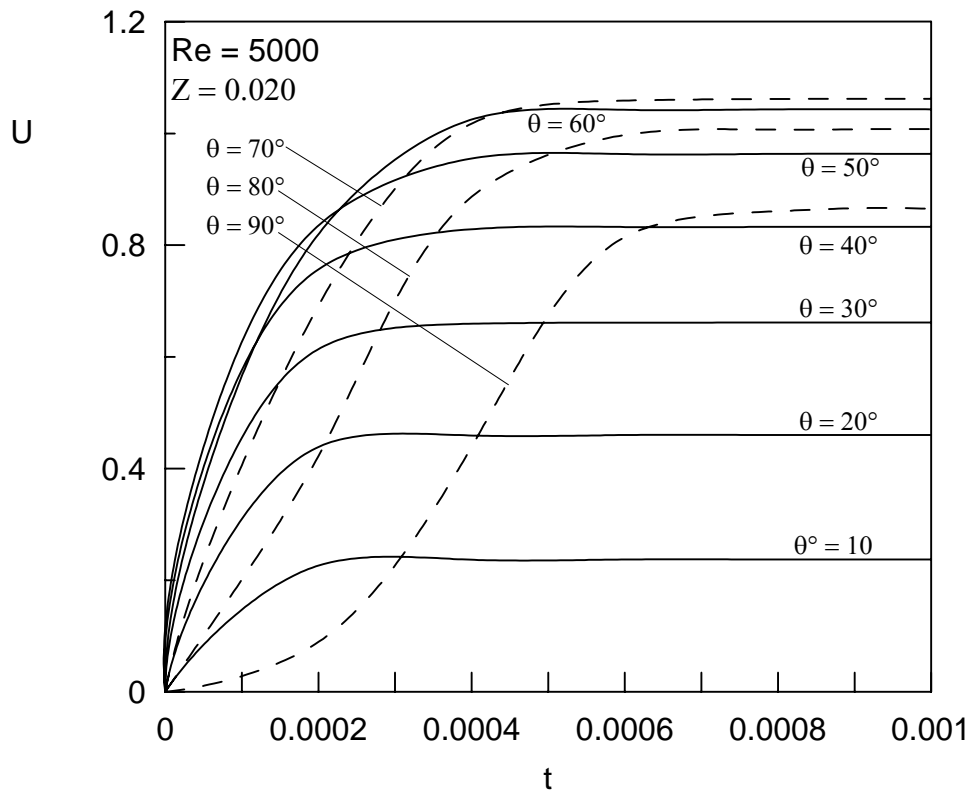


Fig. 6-5: Transient behavior of meridional velocity for $Re = 5000$ and $Z = 0.020$ at different angles

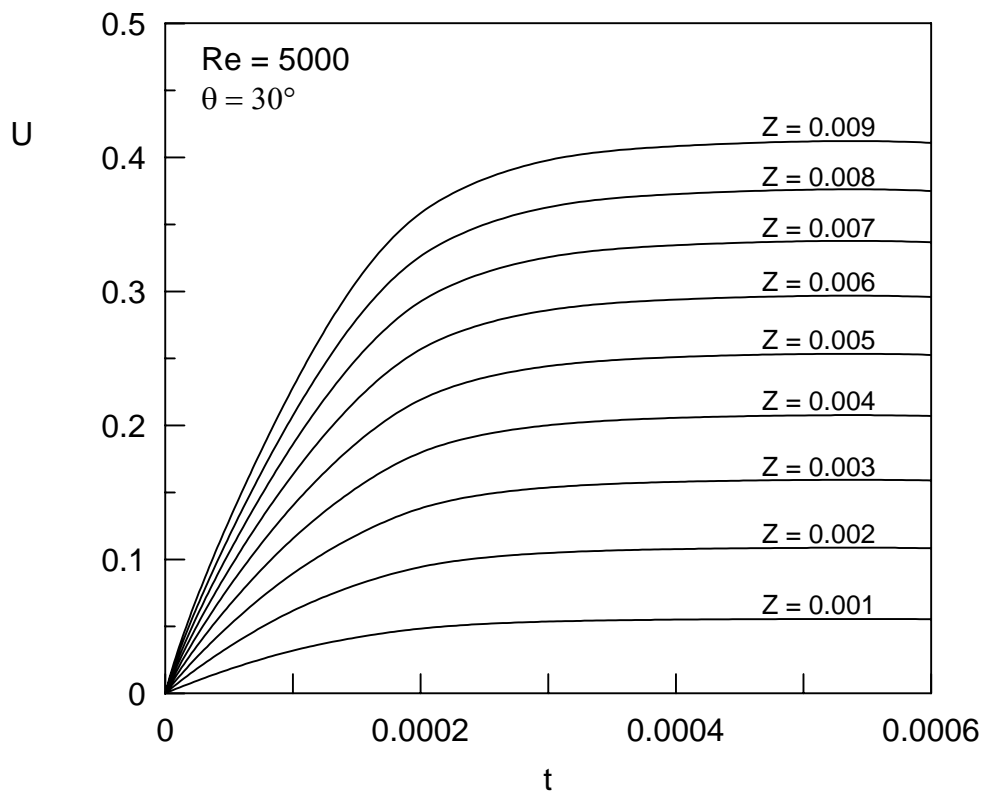


Fig. 6-6: Transient behavior of meridional velocity for $Re = 5000$ and $\theta = 30^\circ$ at different radial locations

6.3 Radial Velocity Profiles

Figures 6-7a, 6-7b and 6-7c show the transient development of the radial velocity component W for $Re = 5000$ and at three different meridional angles ($\theta = 30^\circ$, $\theta = 60^\circ$ and $\theta = 90^\circ$). It is clear that all of these profiles start with a zero value at the surface of the sphere where there is no suction or blowing. However, they end at different values of radial location (Z) where the numerical solution was terminated when the solution criterion was satisfied. Profiles are negative for meridional angle $\theta < 90^\circ$ while they have positive values for $\theta > 90^\circ$. This behavior shows that the radial component of velocity is pushing the boundary-layer fluid towards the sphere's surface in the accelerated region of the flow. Compared with the W -profiles in the adverse region ($\theta > 90^\circ$) where the tendency changes to suction of the fluid, the radial component of velocity assist increasing the boundary-layer thickness till the maximum thickness is reached at the point where the flow separates.

The same plots are repeated for another Reynolds number ($Re = 10,000$) as shown in Figures 6-6a, 6-6b and 6-6c and the same trend is also shown in these figures. It is worth mentioning, too, that the effect of increasing Reynolds number on the thickness of the hydrodynamics boundary layer is clear in these figures and is viewed for $\theta = 30^\circ$ in Figures 6-7a and 6.8a and for $\theta = 60^\circ$ in Figures 6-7b and 6-8b and finally for $\theta = 90^\circ$ in Figures 6-7c and 6-8c.

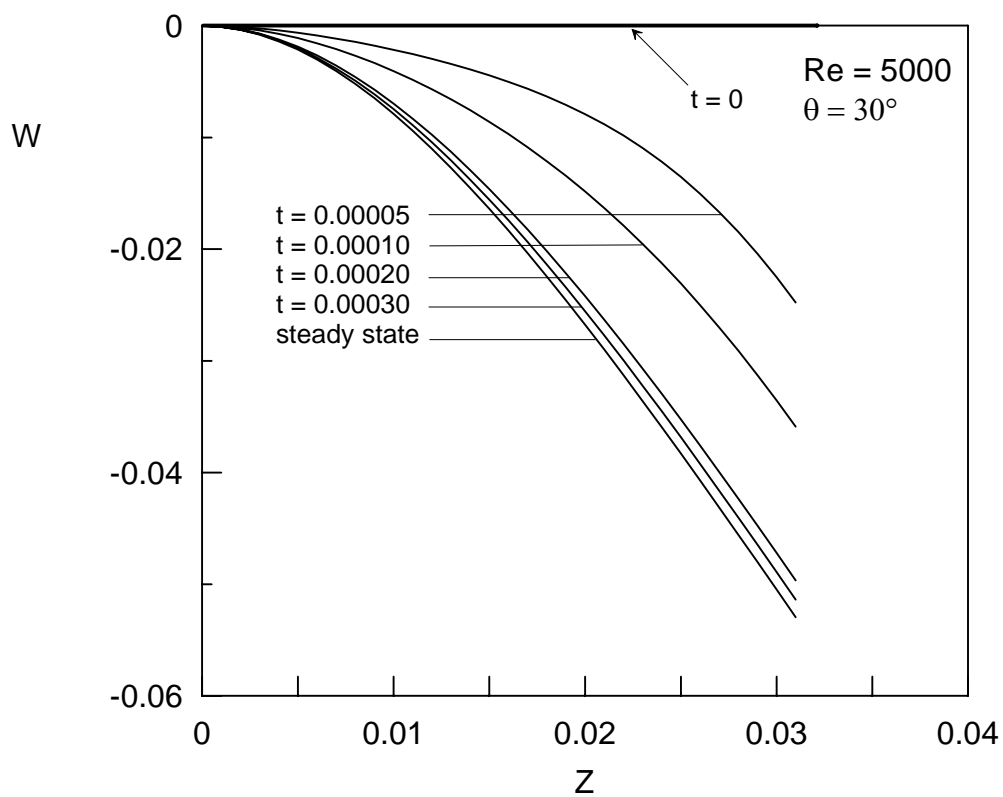


Fig. 6-7a: Transient development of radial velocity for $Re = 5000$, $\theta = 30^\circ$

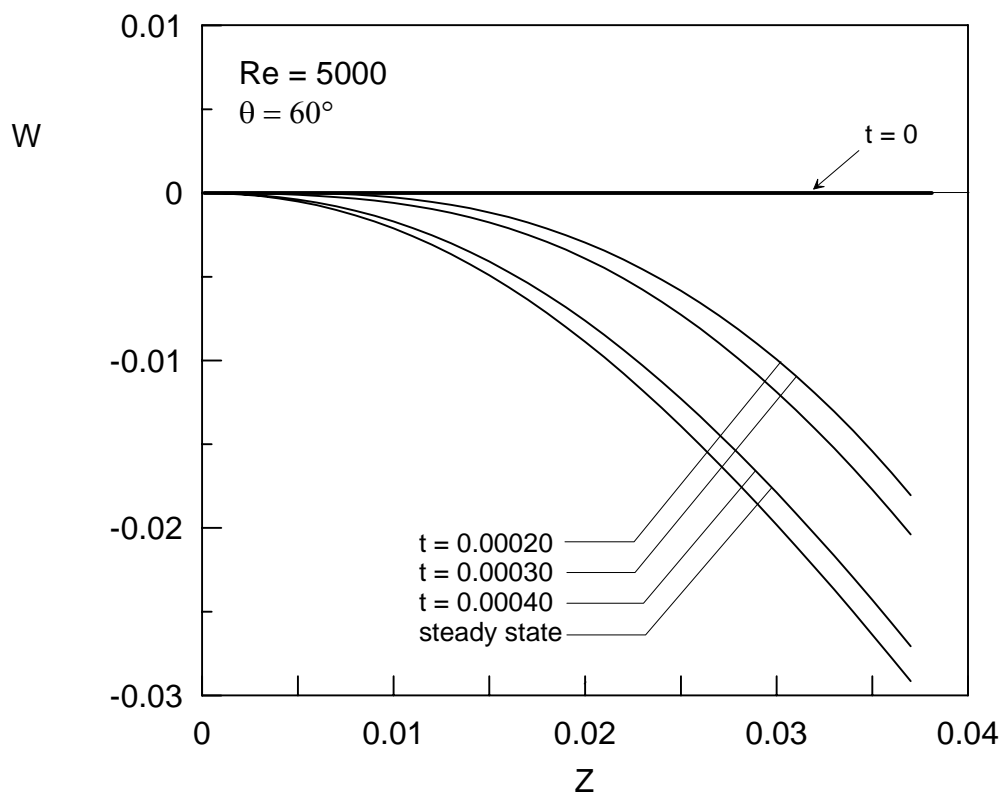


Fig. 6-7b: Transient development of radial velocity for $Re = 5000$, $\theta = 60^\circ$

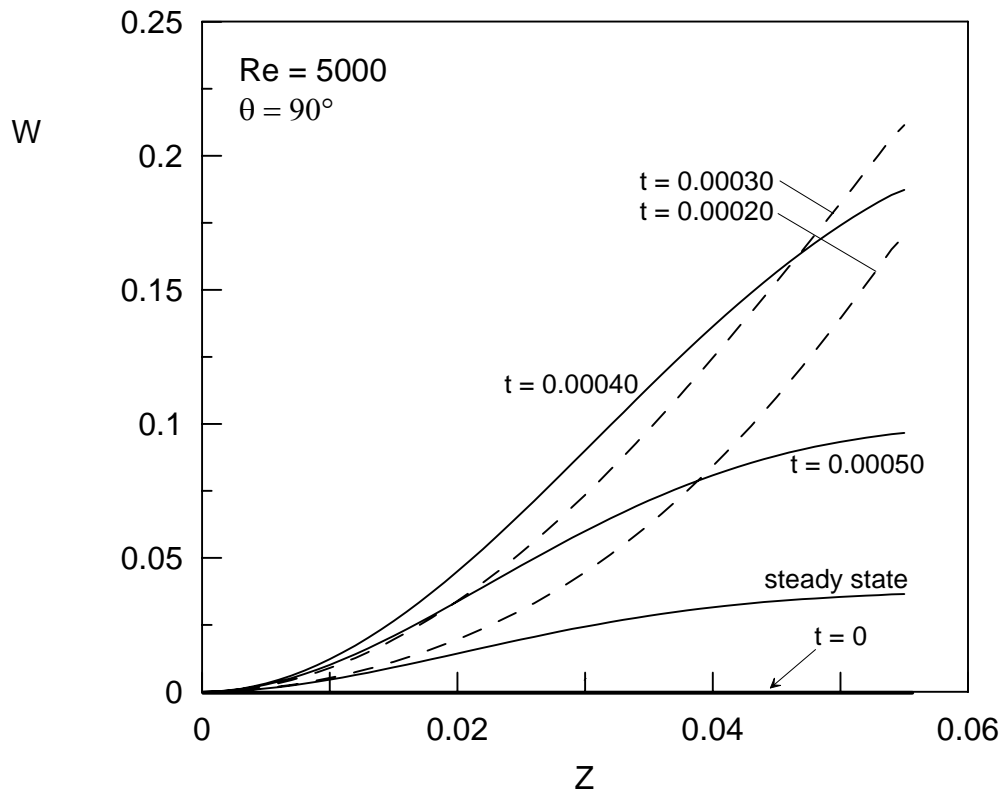


Fig. 6-7c: Transient development of radial velocity for $Re = 5000$, $\theta = 90^\circ$

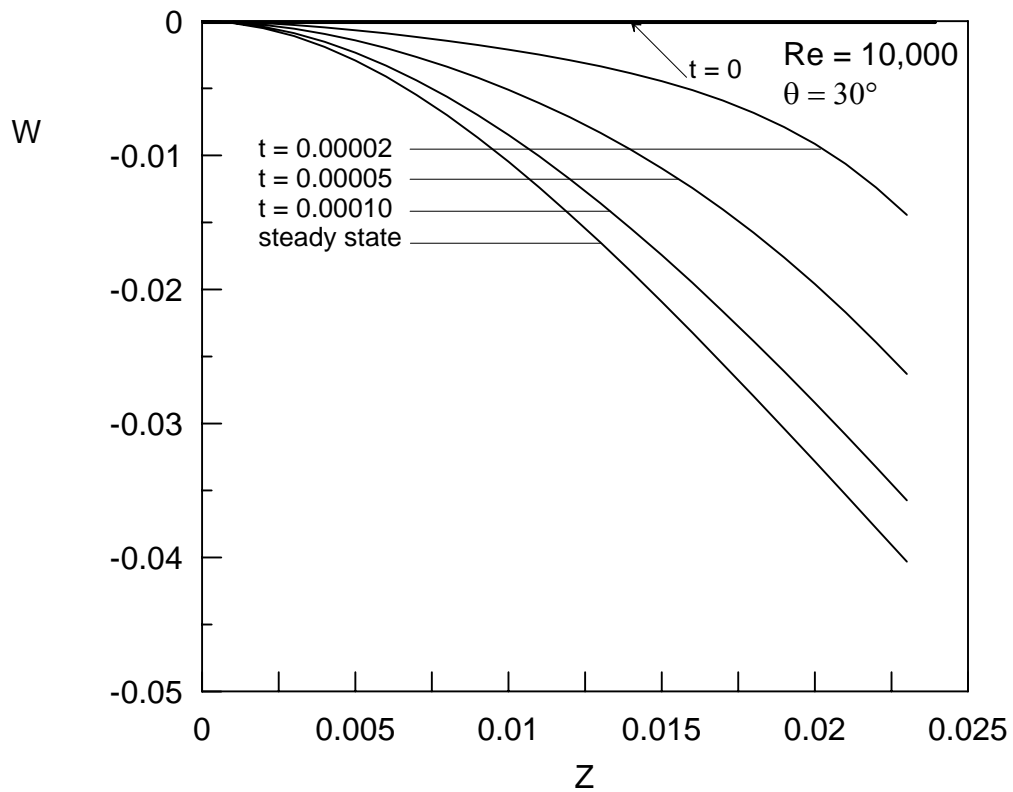


Fig. 6-8a: Transient development of radial velocity for $Re = 10,000$, $\theta = 30^\circ$

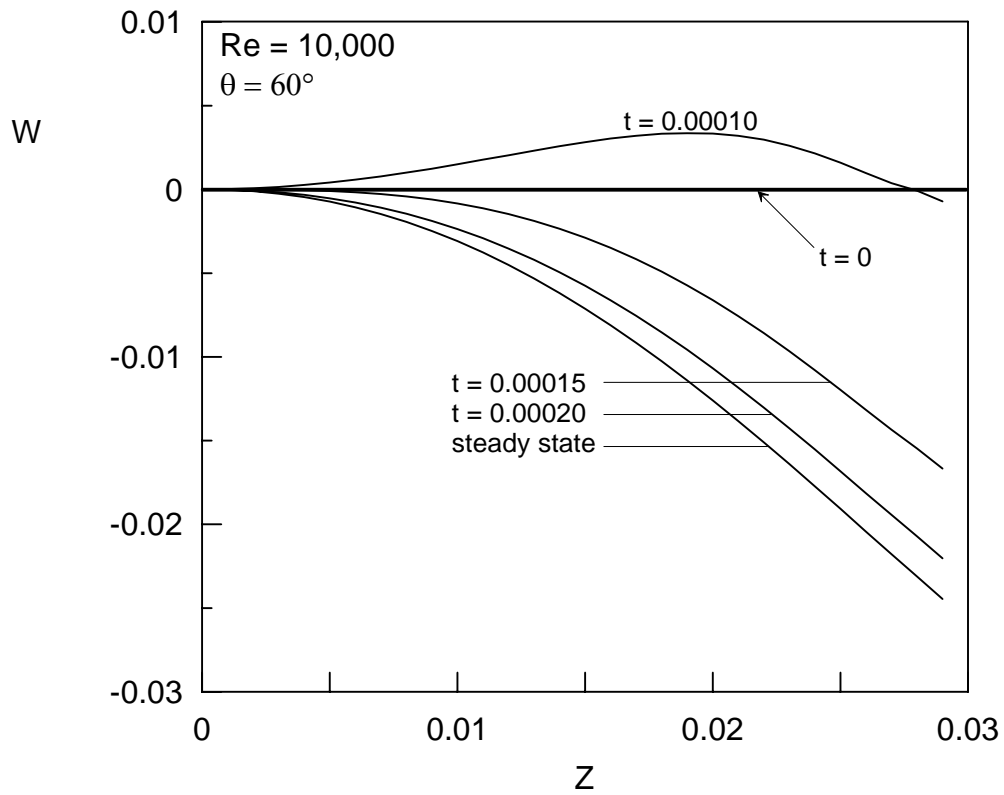


Fig. 6-8b: Transient development of radial velocity for $Re = 10,000$, $\theta = 60^\circ$

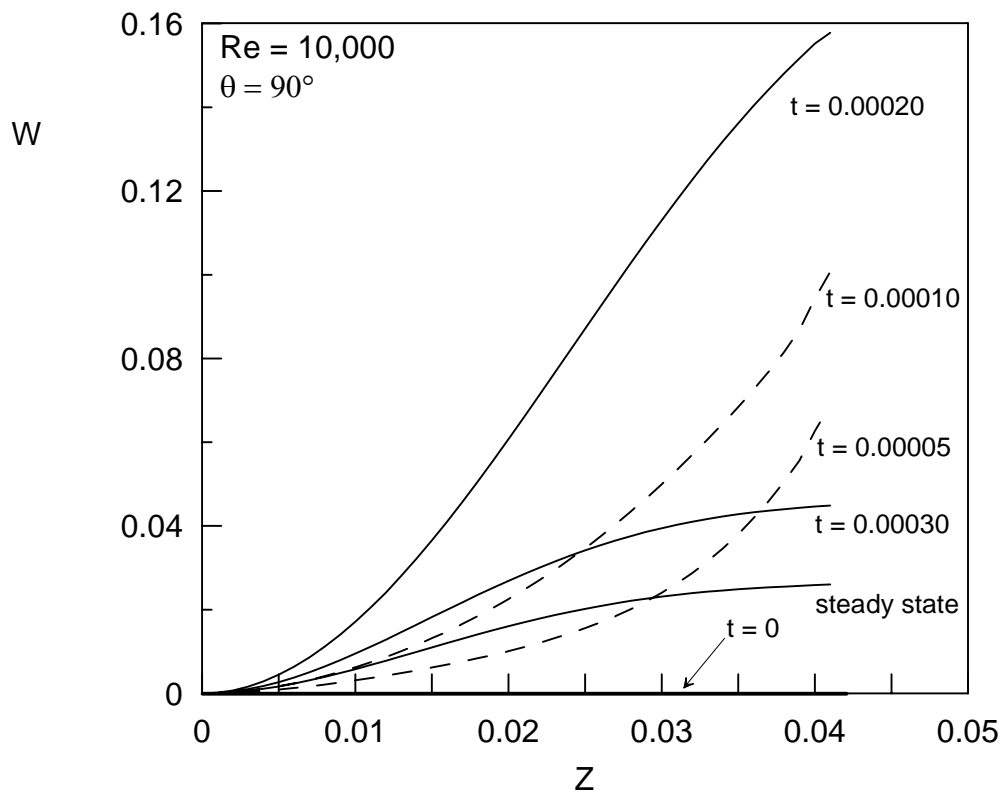


Fig. 6-8c: Transient development of radial velocity for $Re = 10,000$, $\theta = 90^\circ$

For specific values of times ($t = 0.00040$, $t = 0.00070$ and steady state), Figs. 6-9a, 6-9b and 6-9c show the radial velocity profiles at certain meridional angle ($\theta = 60^\circ$) for three different values of Reynolds number ($Re = 1000$, $Re = 5000$ and $Re = 10,000$). Increasing the Reynolds number always has the effect of decreasing the boundary-layer thickness as illustrated previously. Hence the smallest boundary-layer thickness corresponds to the highest value of Reynolds number ($Re = 10,000$), while the highest thickness was reported for the lower value of Reynolds number used ($Re = 1000$).

Figures 6-10a, 6-10b and 6-10c show the radial velocity profile for different meridional angles $\theta = 30^\circ$, $\theta = 60^\circ$ and $\theta = 90^\circ$ at different time steps $t = 0.00040$, $t = 0.00070$ and steady state, respectively. They are plotted for a fixed value of Reynolds number ($Re = 5000$). It is clear from the figures that the boundary-layer thickness increases from its zero value at the front stagnation point until it reaches its maximum value at the point of flow separation.

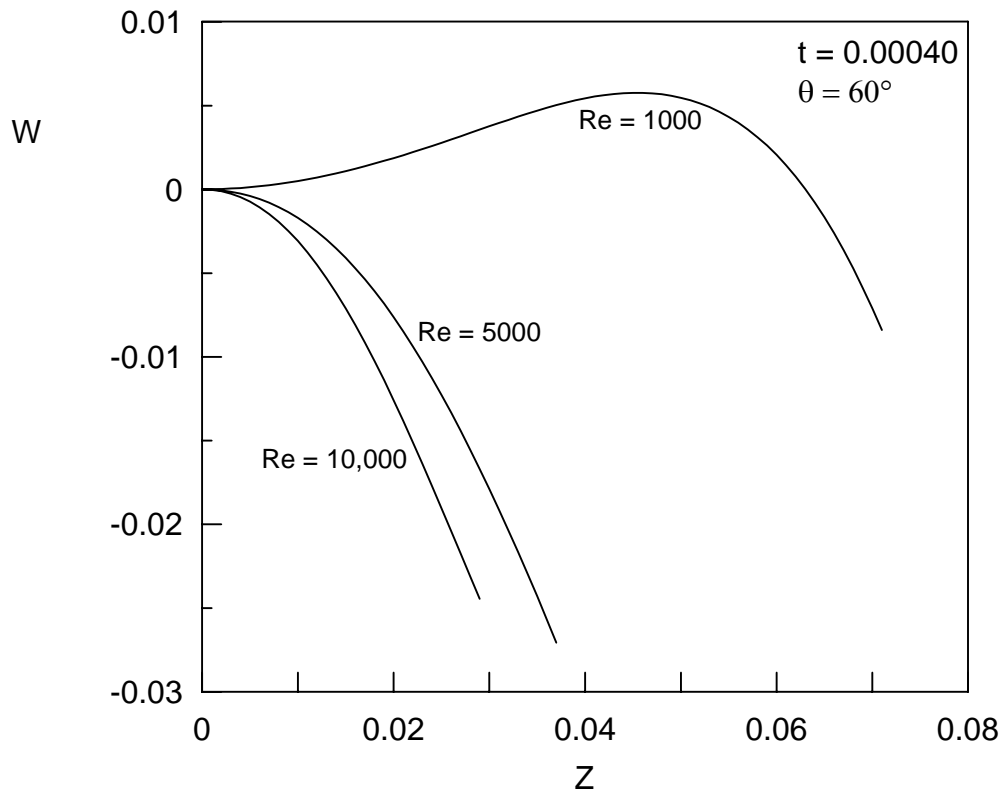


Fig. 6-9a: Radial velocity at $\theta = 60^\circ$ for different Reynolds numbers, $t = 0.00040$

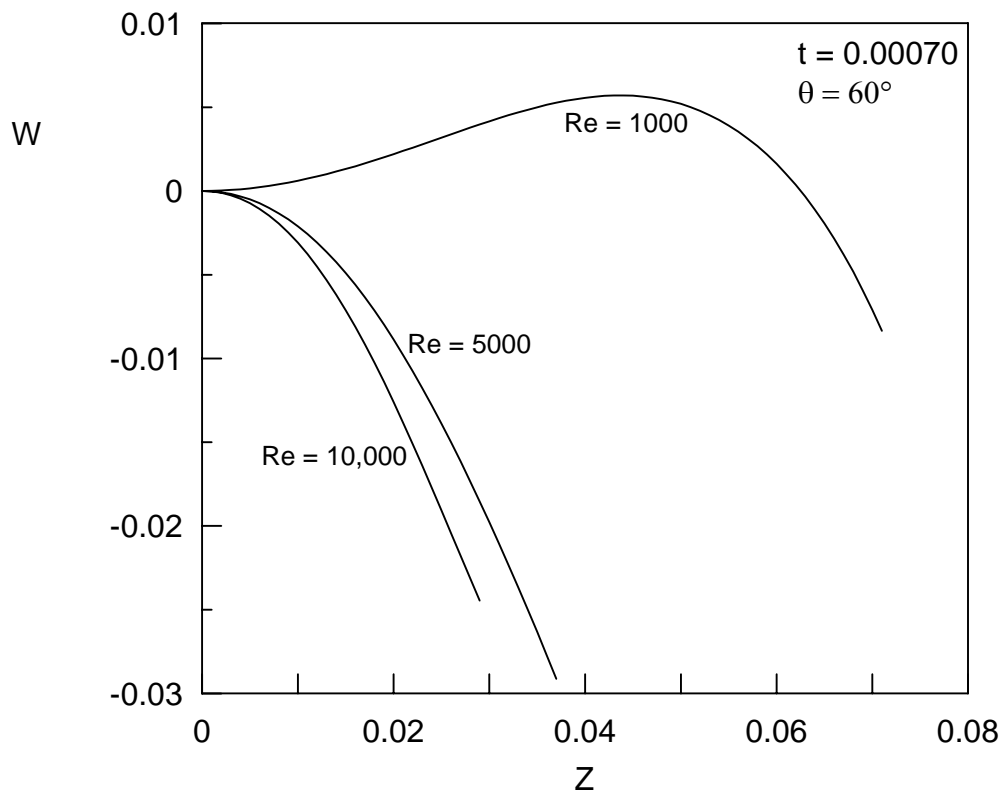


Fig. 6-9b: Radial velocity at $\theta = 60^\circ$ for different Reynolds numbers, $t = 0.00070$

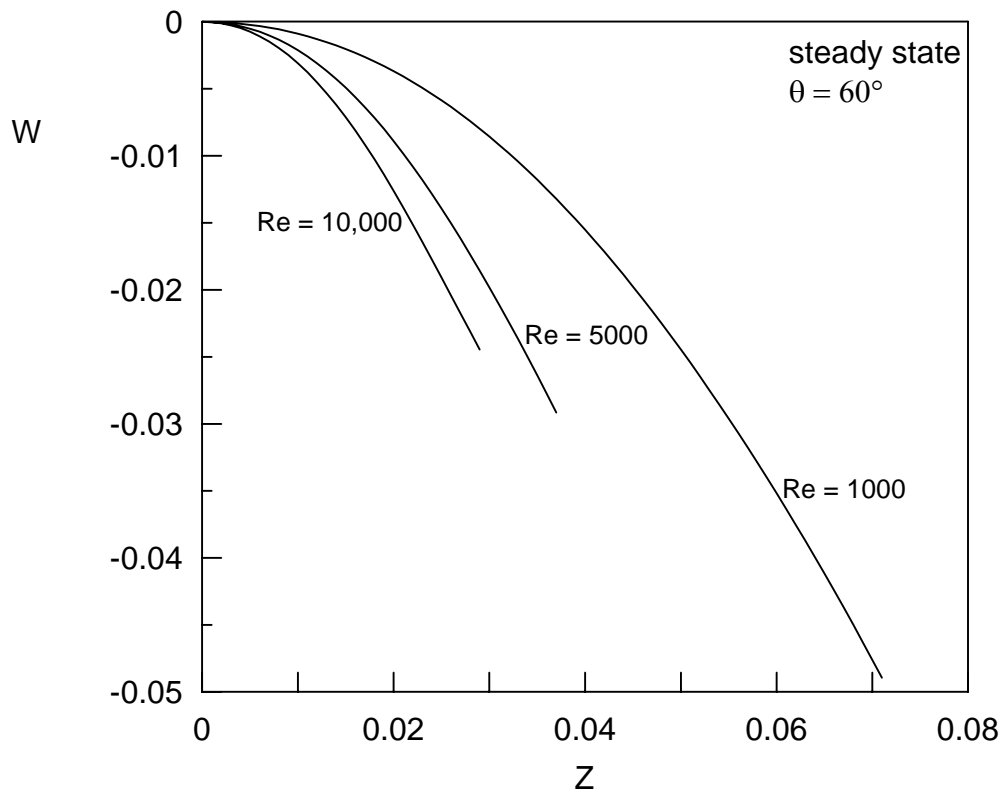


Fig. 6-9c: Radial velocity at $\theta = 60^\circ$ for different Reynolds numbers at steady state

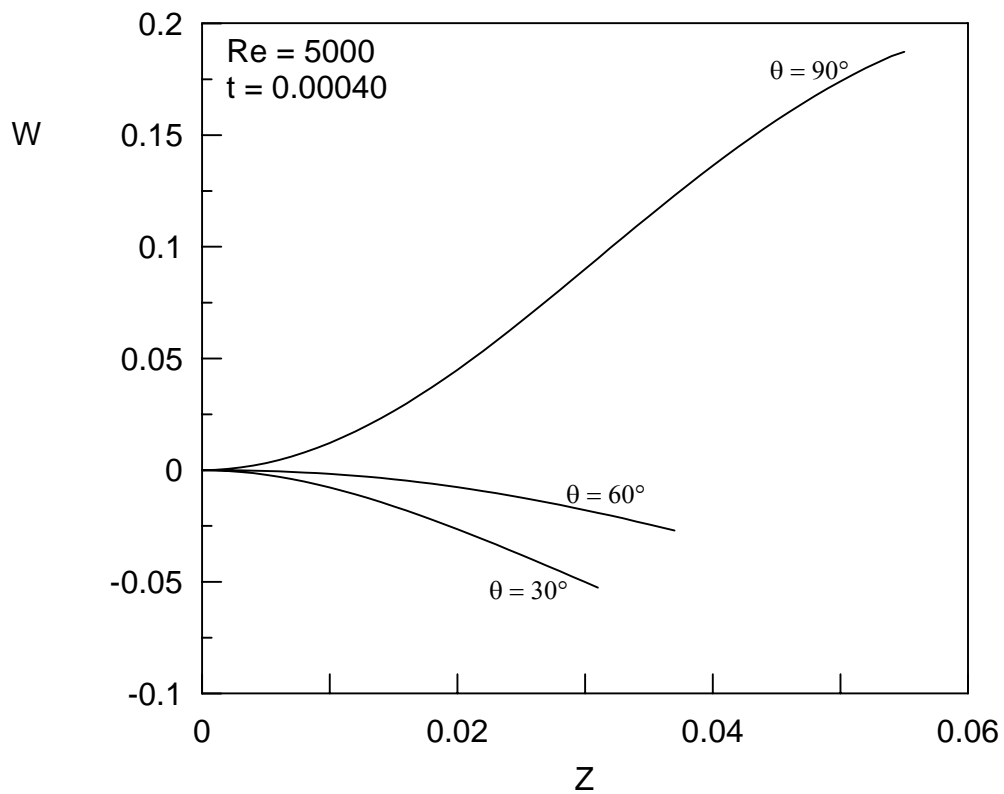
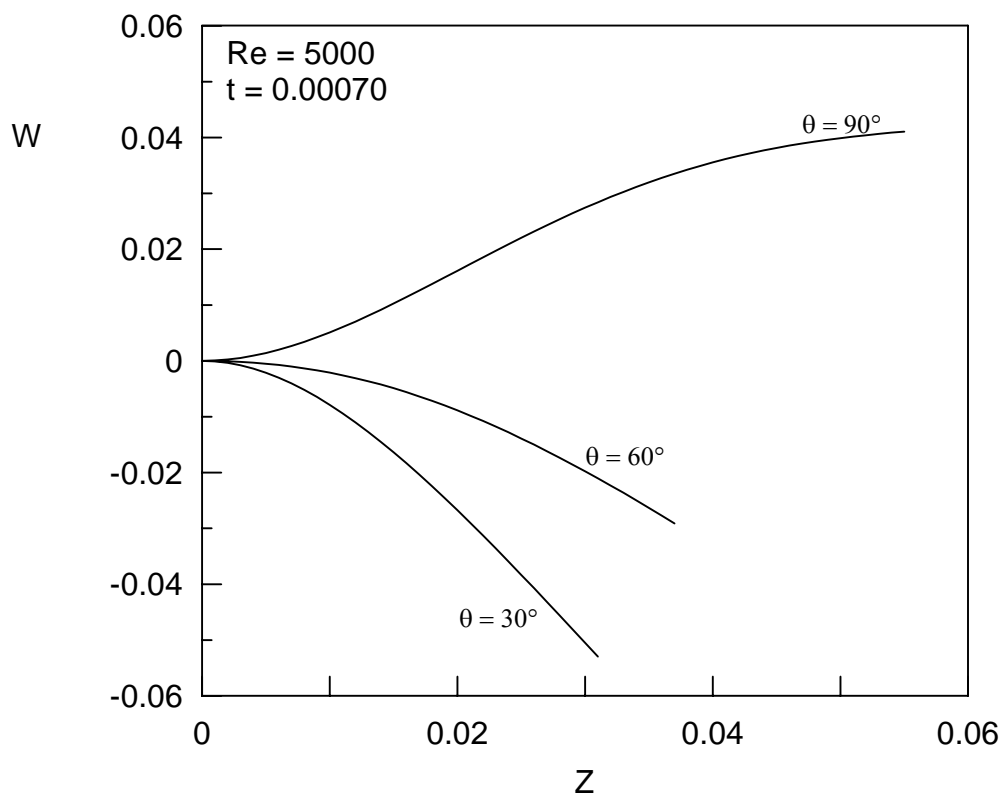
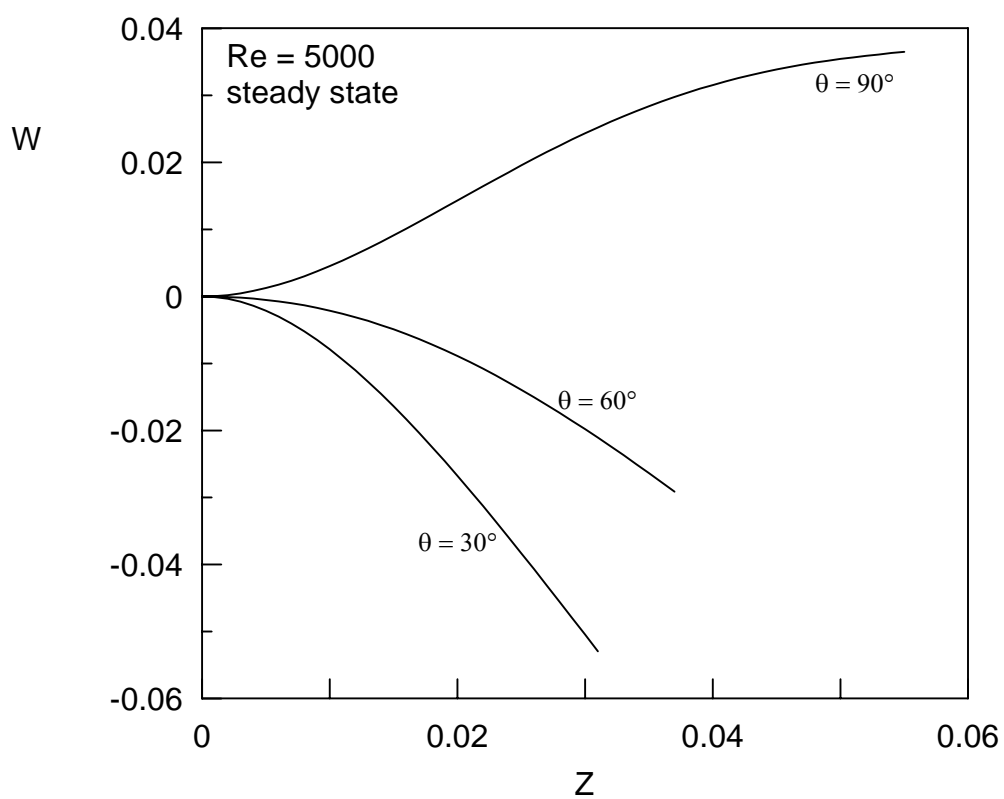


Fig. 6-10a: Radial velocity for $Re = 5000$ at different angles, $t = 0.00040$

Fig. 6-10b: Radial velocity for $Re = 5000$ at different angles, $t = 0.00070$ Fig. 6-10c: Radial velocity for $Re = 5000$ at different angles at steady state

CHAPTER VII

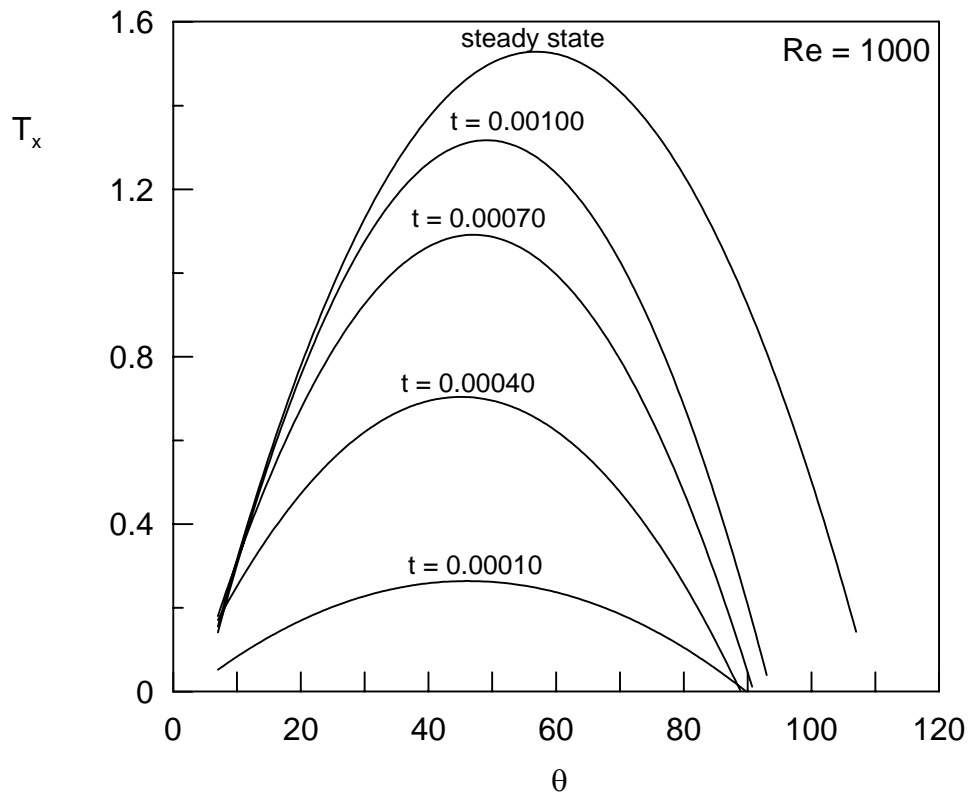
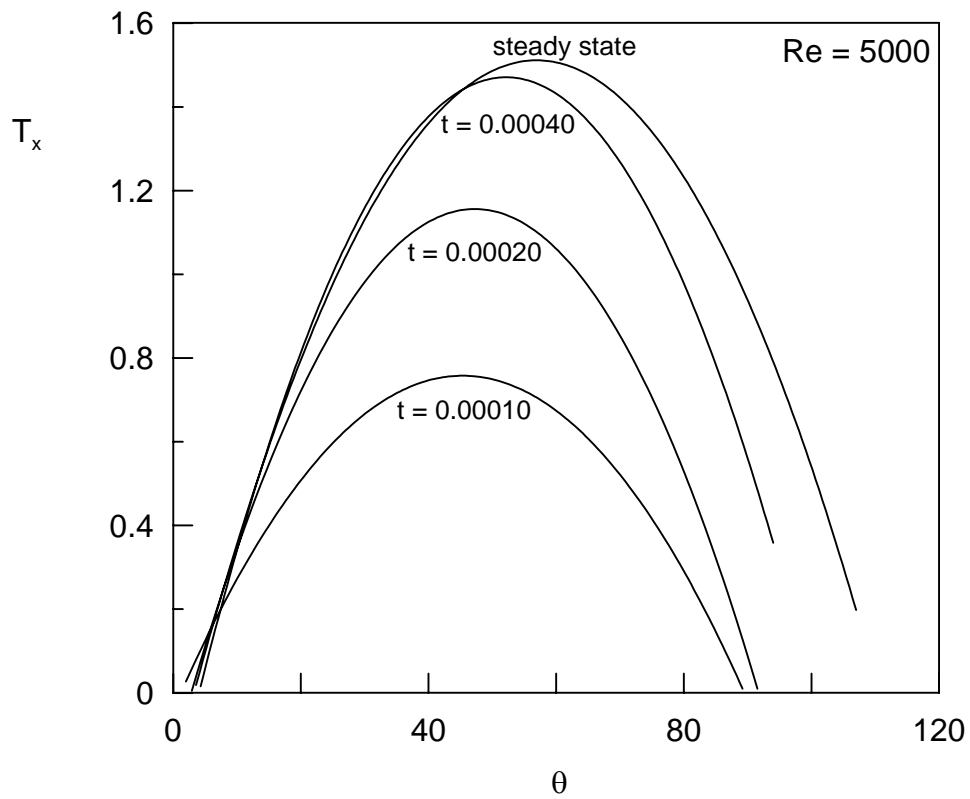
ENGINEERING PARAMETERS

7.1 Introduction

In this chapter, the results of calculating engineering parameters of interest are presented for various values of Reynolds number. These parameters include the shear stress at the surface of the sphere, the friction coefficient, the drag coefficient and the surface vorticity. Other parameters such as the variation of flow separation angle with time and the time required to reach steady state condition are also reported, in this chapter, for a wide range of Reynolds number.

7.2 Surface Shear Stress

Figures 7-1a, 7-1b and 7-1c show the transient development of the dimensionless shear stress around the sphere plotted for three values of Reynolds number $Re = 1000$, 5000 and $10,000$, respectively. At early time, the values of shear stress around the sphere are low due to low velocity within the boundary-layer. As time passes and due to momentum diffusion within the boundary-layer, the velocity increases which results in a corresponding increase in the shear stress until the steady state condition is reached.

Fig. 7-1a: Transient development of the surface shear stress for $Re = 1000$ Fig. 7-1b: Transient development of the surface shear stress for $Re = 5000$

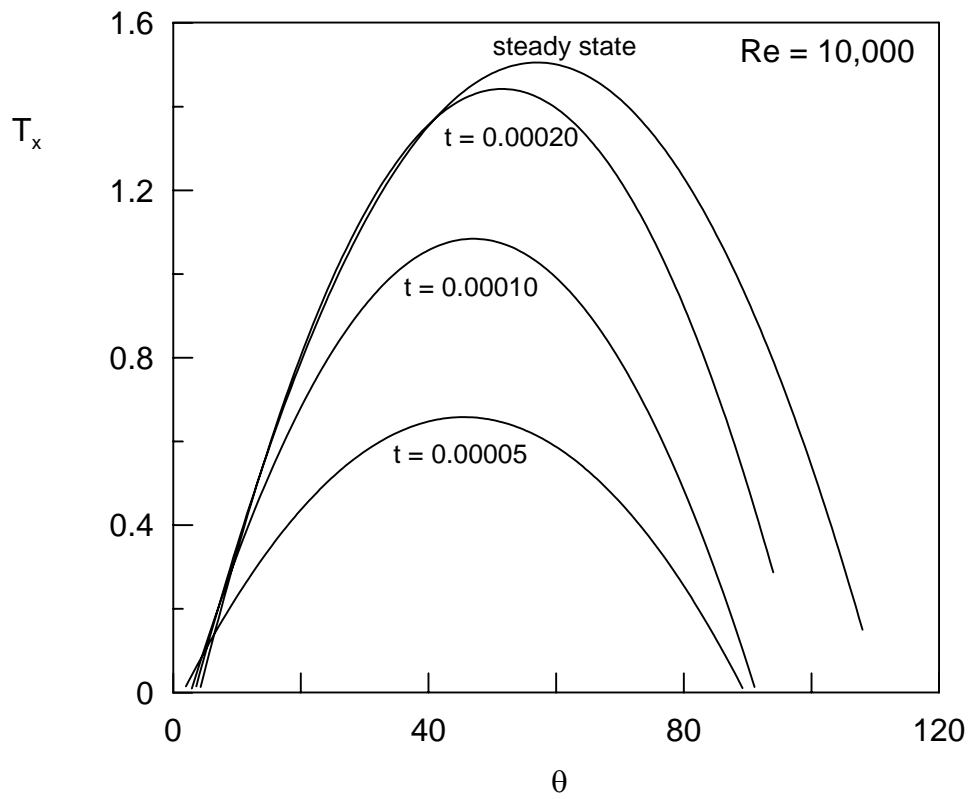


Fig. 7-1c: Transient development of the surface shear stress for $Re = 10,000$

These figures also show that steady state condition is reached earlier for high Reynolds numbers. That is, less time is noticed for $Re = 10,000$ compared to $Re = 5000$, whereas the case of $Re = 1000$ required the largest time to reach steady state. This is illustrated clearly in Figure 7-2 where the effect of Reynolds number on the surface shear stress at a given time ($t = 0.00040$) is shown. It is clear from the figure that increasing the Reynolds number has the effect of increasing the shear stress around the sphere, due to the increased velocity gradient at higher Reynolds number, until the steady state distribution is attained.

The transient behavior of the surface shear stress for $Re = 5000$ and $Z = 0.020$ plotted at various meridional angles is shown in Figure 7-3. It is clear from the figure that as the time elapses ($t > 0$), the surface shear stresses increase until the steady state condition of flow is reached. The figure also shows that as the meridional angle increases, the surface shear stress values increase due to the increase in meridional velocities. However, as the meridional angle approaches the separation point, the steady state values of the shear stress start decreasing. This behavior is related directly to meridional velocities behavior which was explained in page 46.

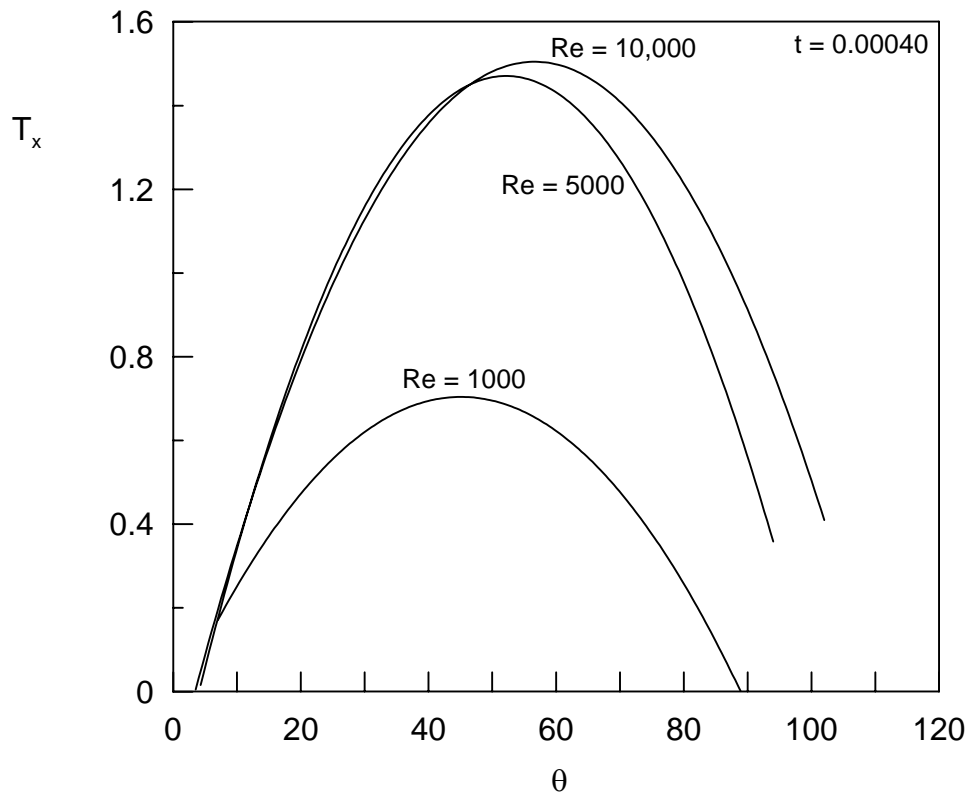


Figure 7-2: Effect of Reynolds number on the surface shear stress at a given time ($t = 0.00040$)

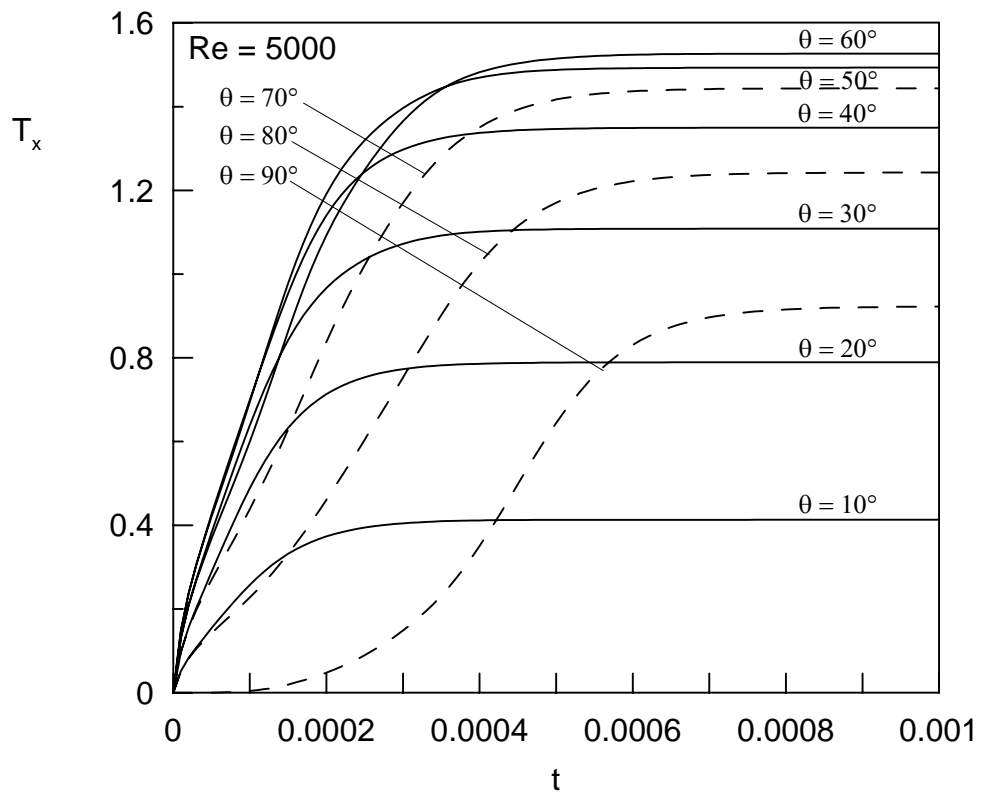


Figure 7-3: Transient behavior of surface shear stress for $Re = 5000$ at different angles

7.3 Friction Coefficient

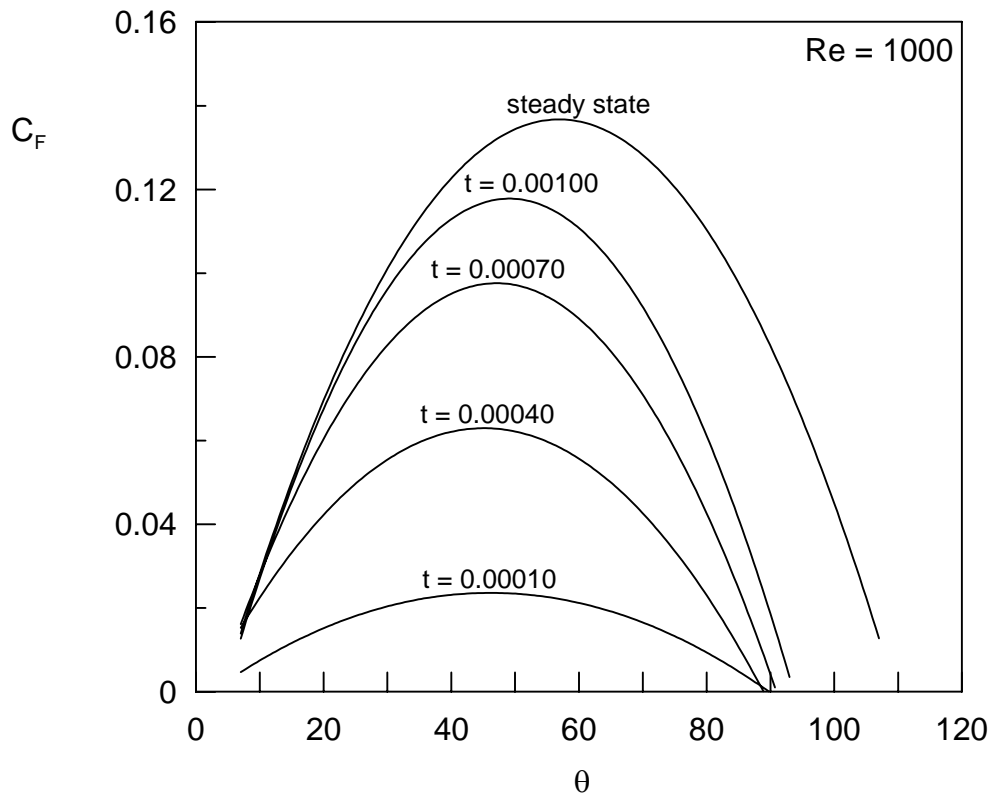
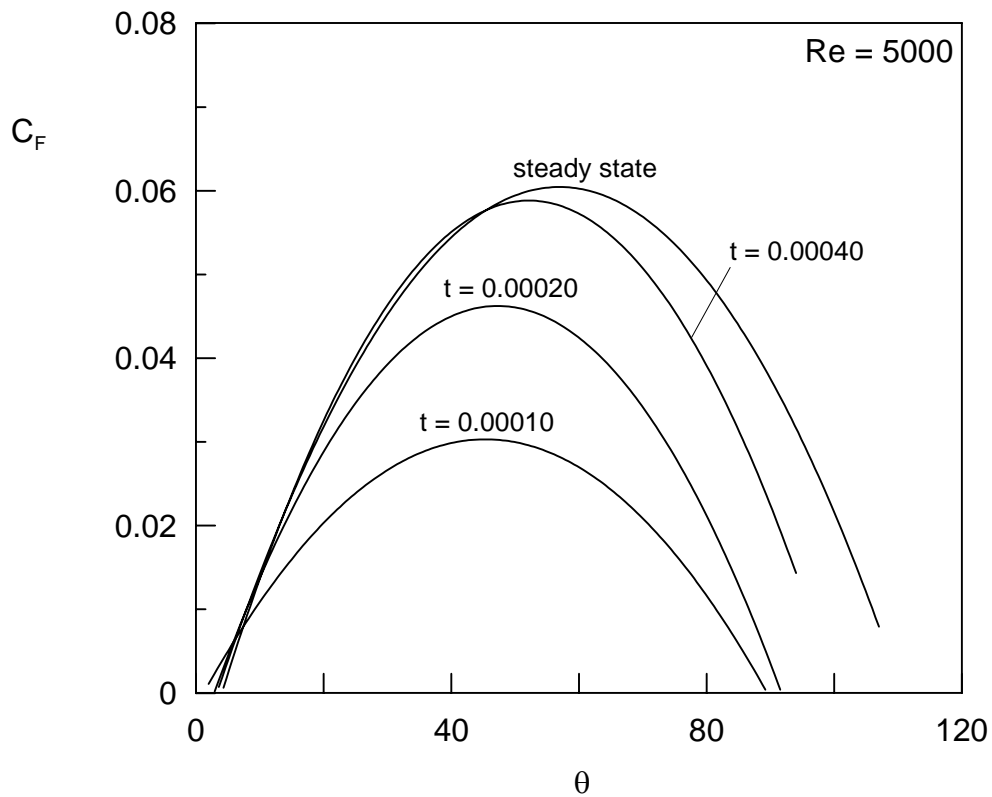
Figures 7-4a, 7-4b and 7-4c show the transient development of friction coefficient plotted for three values of Reynolds number $Re = 1000, 5000$ and $10,000$, respectively. At early time, the values of friction coefficient are low due to low shear stress values at the surface of the sphere at that incident of time. As time passes and due to increasing the shear stress (as described in the section 7-2), the coefficient of friction increases accordingly until the steady state condition is reached.

The effect of Reynolds number on the coefficient of friction at a given time ($t = 0.00040$) is shown in Figure 7-5. It is clear from the figure that increasing the Reynolds number has the effect of decreasing the values of friction coefficient although the shear stress increases with increasing Reynolds number. This is because the dimensionless value of the coefficient is the result of dividing the shear stress by the velocity pressure that includes square of the velocity. Increasing Reynolds number would increase U_∞ significantly and hence decreases the coefficient of friction.

7.4 Drag Coefficient

Figure 7-6 shows the variation of the drag coefficient with time plotted for three values of Reynolds number ($Re = 1000, 5000$ and $10,000$). It is clear from the figure that as time passes, the drag coefficient increases until the steady state condition of flow is reached. The figure also shows that increasing the Reynolds number results in decreasing the steady state coefficient of drag. This is because the dimensionless value of the drag coefficient includes a term (i. e. R) which is inversely proportional to Reynolds number.

A comparison between the steady state drag coefficient of the current investigation at various Reynolds numbers and the results of El-Shaarawi et al. work [5] is shown in Table 7-1. The two results are almost the same.

Fig. 7-4a: Transient development of friction coefficient for $Re = 1000$ Fig. 7-4b: Transient development of friction coefficient for $Re = 5000$

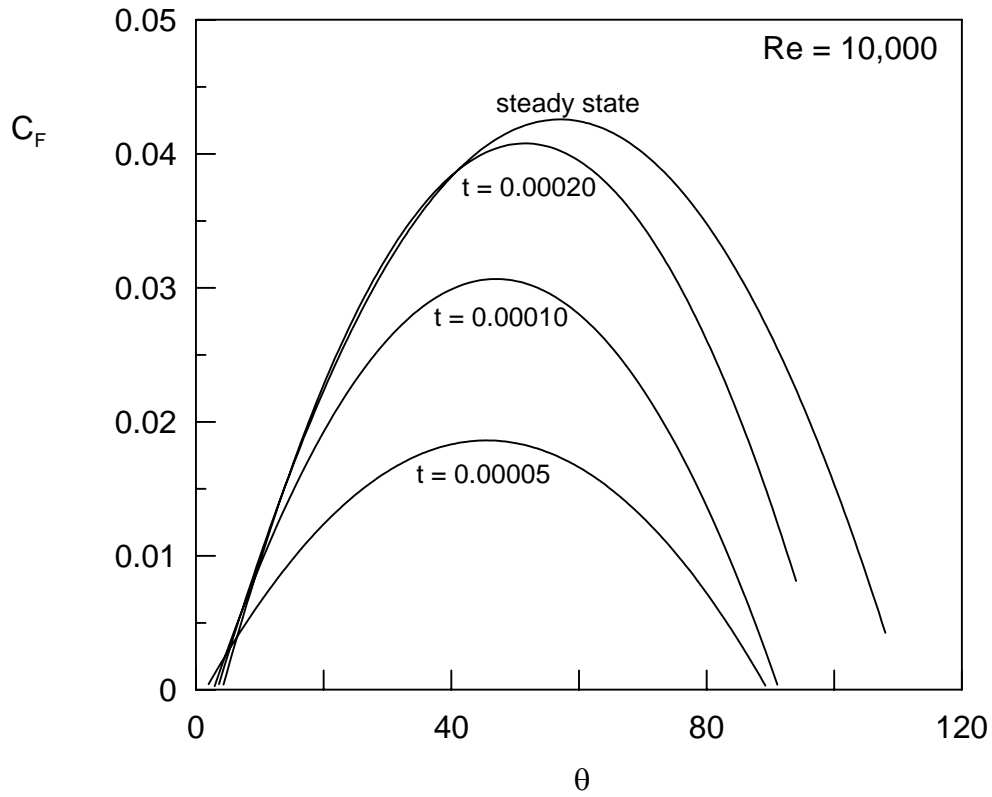


Fig. 7-4c: Transient development of friction coefficient for $Re = 10,000$

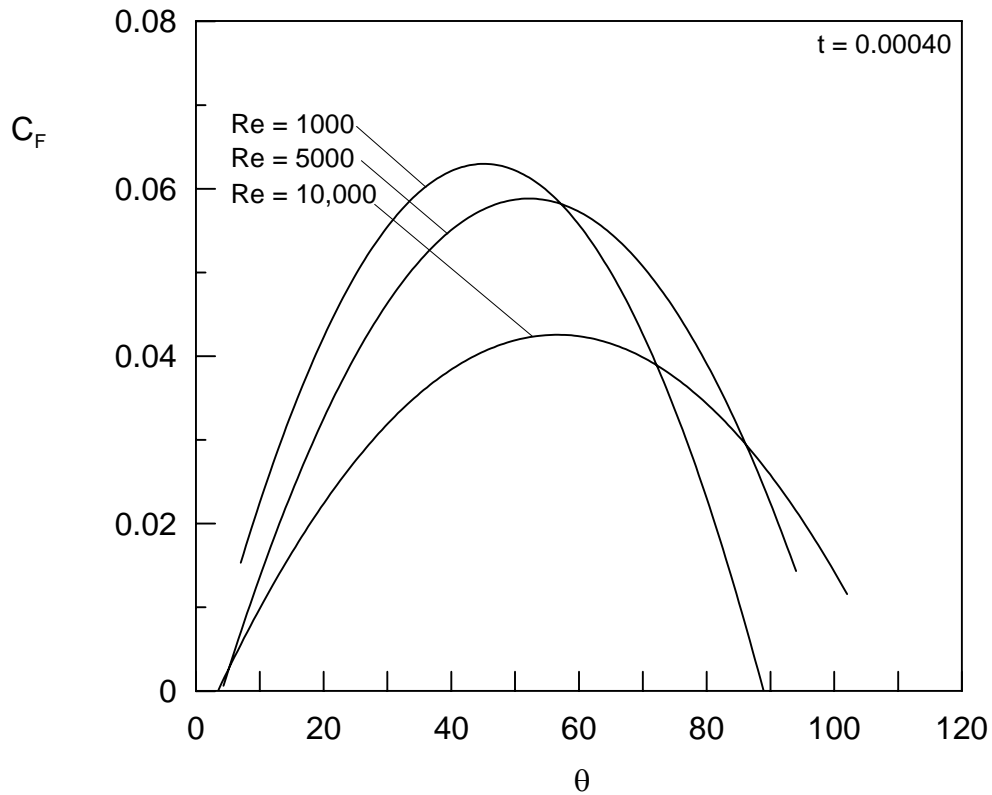


Fig. 7-5: Effect of Reynolds number on the friction coefficient at a given time ($t = 0.00040$)

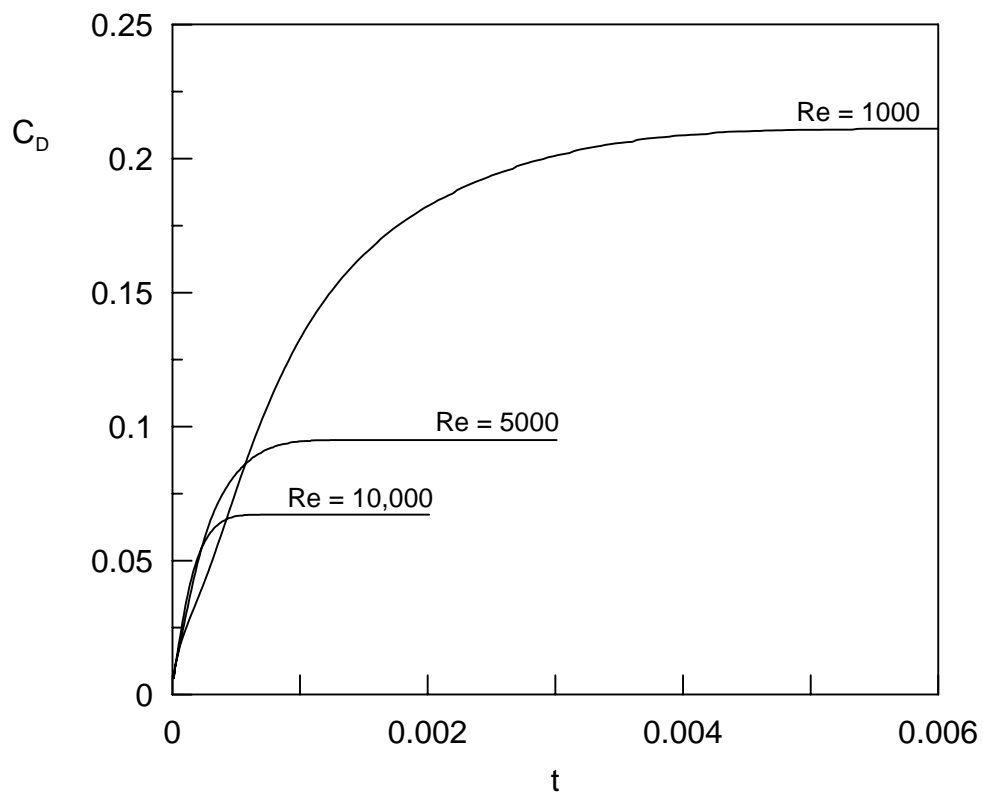


Fig. 7-6: Transient behavior of drag coefficient at different values of Reynolds number

Table 7-1: Comparison between the steady state drag coefficient of the present analysis and the results of El-Shaarawi et al. work [5]

Re	C_D	
	Present analysis	El-Shaarawi et al.work [5]
1000	0.21123	0.21123
3000	0.12250	0.12252
5000	0.09496	0.09498
7000	0.08027	0.08030
10,000	0.06716	0.06716

7.5 Surface Vorticity

Figure 7-7 shows the transient development of the vorticity at the surface of the sphere along the meridional direction plotted for $Re = 1000$. At early time, the values of surface vorticity are low due to low rotation of fluid particles near the sphere surface. As time elapses and due to momentum diffusion within the boundary-layer, the rotation of fluid particles increases which results in a corresponding increase in the surface vorticity until the steady state condition is reached. A comparison between the steady state surface vorticity of the current work at Reynolds no of 100 and the boundary-layer analysis by Hamielec et al. [1] is shown in Figure 7-8. A good agreement between the two results is shown in the figure.

7.6 Variation of Separation Angle with Time

Figure 7-9 shows the variation of the angle of flow separation with time plotted for three values of Reynolds number ($Re = 1000, 5000$ and $10,000$). The angle of external flow separation increases with time since as the time passes, the meridional velocity increases and hence the boundary layer thickness decreases making separation occur at higher values of θ . This figure shows also the effect of Reynolds number. Increasing the Reynolds number causes the flow to separate at earlier time since it requires less time to reach steady state condition. The figure also shows that increasing Reynolds number increases the angle at which flow separates. This is due to thinning the boundary layer at high Reynolds numbers.

7.7 Time to Reach Steady State

Figure 7-10 shows the effect of Reynolds number on the time required to reach steady state. It is clear from the figure that increasing the Reynolds number decreases the time required to reach the steady state condition. This is due to higher velocities in the boundary-layer resulting from increasing Reynolds number.

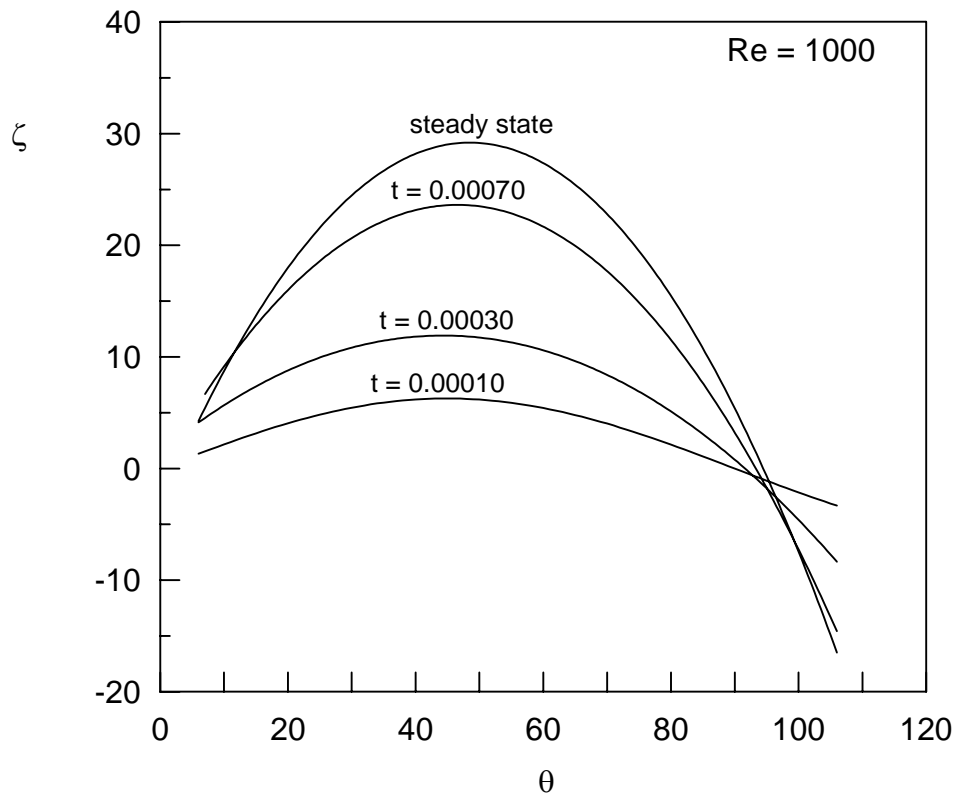


Fig. 7-7: Transient development of surface vorticity for $Re = 1000$

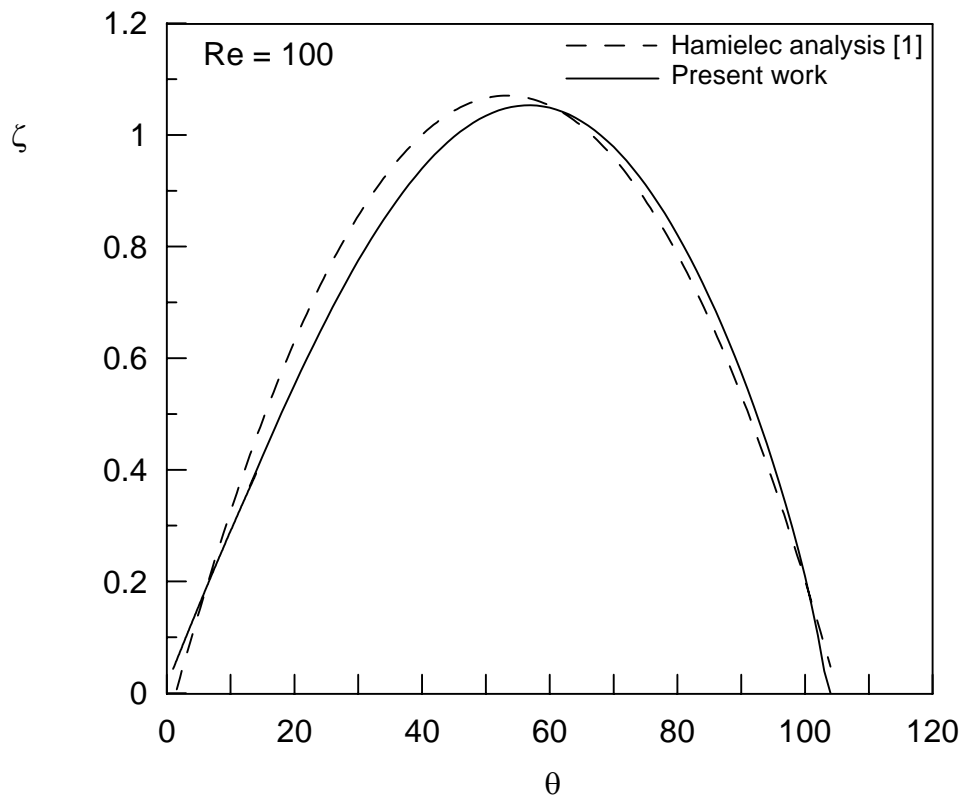


Fig. 7-8: Steady state surface vorticity compared with boundary-layer solution of [1]

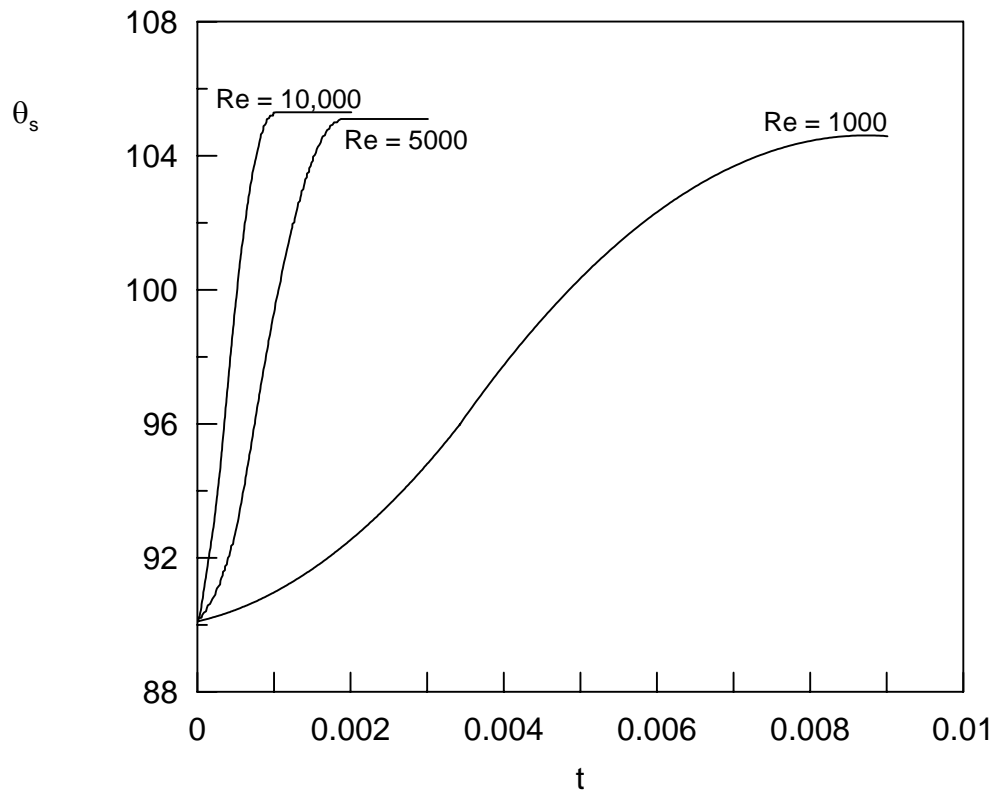


Fig. 7-9: Effect of Reynolds number on the variation of separation angle with time

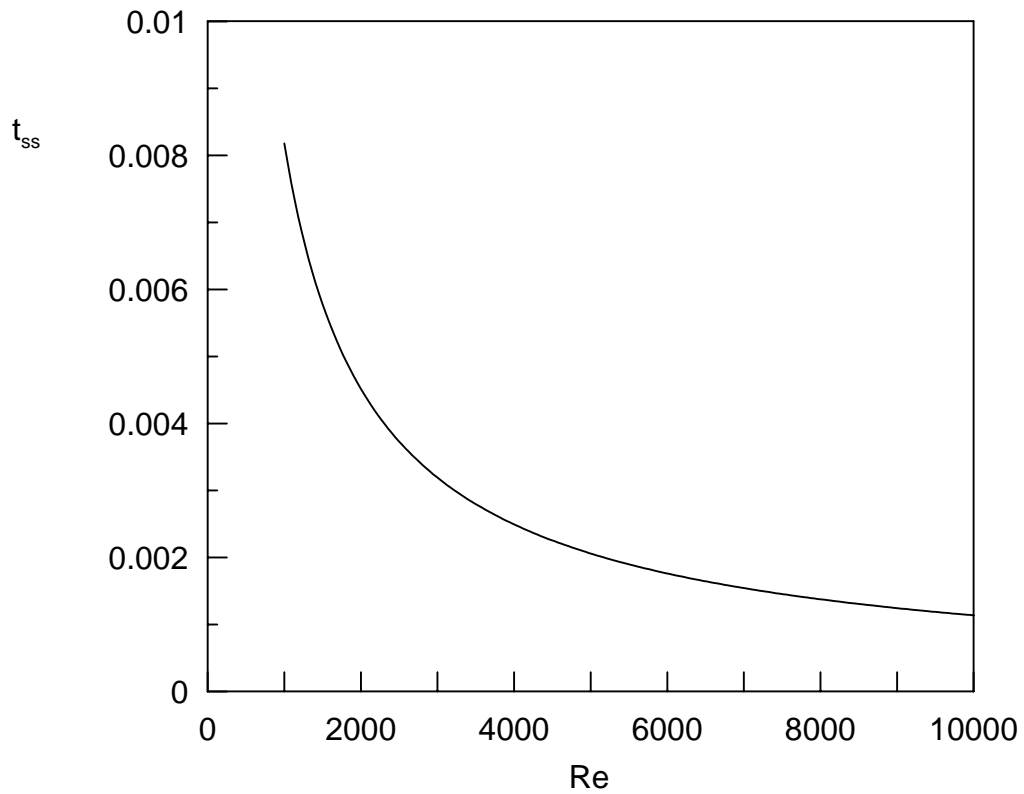


Fig. 7-10: Effect of Reynolds number on the time required to reach steady state

CHAPTER VIII

CONCLUSIONS & RECOMMENDATIONS

8.1 Conclusions

A finite-difference scheme has been developed and successfully used to solve the 3-D boundary-layer equations governing the unsteady impulsively started fluid flow about a solid sphere. The present scheme has succeeded in obtaining solutions for considerably larger values of Reynolds number. For the studied range $1000 \leq Re \leq 10,000$, results are presented for the meridional and radial velocity profiles, the surface shear stress, the friction coefficient, the drag coefficient and the external flow separation angle. The time to reach steady state is also obtained and presented.

The obtained results show that the Reynolds number has a significant effect on the flow characteristics around the sphere. Increasing the Reynolds number results in reducing the time required to reach the steady state condition, increasing the shear stress at the sphere's surface and decreasing both the drag and friction coefficients. The exterior flow separation angle was found to increase with time until the steady state condition is reached and its value increases with increasing the Reynolds number. It was also found that the drag coefficient increases with time until the steady state condition is achieved

and its value decreases as the Reynolds number increases. A comparison between the computed values of drag coefficient and surface vorticity with some data found in the literature was carried out and good agreement between the present analysis and these values was obtained.

8.2 Recommendations for Future Work

It is recommended to extend the present work to cover the following cases;

1. Rotating sphere.
2. Forced and mixed convection heat/mass transfer.

REFERENCES

1. Jenson, V.J., "Viscous Flow Around a Sphere at Low Reynolds Numbers (<40)", *Proc. Roy. Soc. A* 249, 246-266, 1956.
2. Dinnis, S.C.R. and Walker, J.D.A., "Calculation of the Steady Flow Past a Sphere at Low and Moderate Reynolds Numbers", *J. Fluid Mech.*, Vol 49, Part 4, pp. 771-789, 1971.
3. Hamielec, A.E., Hoffman, T.W. and Ross, L.L., "Numerical Solution of the Navier-Stokes Equation for Flow Past Spheres: Part I. Viscous Flow Around Spheres with and Without Radial Mass Efflux", *A.I.Ch.E. Journal*, Vol. 13, No. 2, pp. 212-219, 1967.
4. Pruppacher, H.R., Le Clair, B.P. and Hamielec, A.E., "Some Relations Between Drag and Flow Pattern of Viscous Flow Past Sphere and Cylinder at Low and Intermediate Reynolds Numbers", *Journal of Fluid Mechanics*, Vol. 44, Part 4, pp. 781-790, 1970.
5. El-Shaarawi, M.A.I., EL-Refaie, M.F. and El-Bedeawi, S.A., "Numerical Solution of Laminar Boundary Layer Flow About a Rotating Sphere in an Axial Stream", *Journal of Fluids Engineering, Transactions of the ASME*, Vol. 107, pp. 97-104, 1985.
6. Rimon, Y. and Cheng, S.I., "Numerical Solution of a Uniform Flow Over a Sphere at Intermediate Reynolds Numbers", *The Physics of Fluids*, Vol. 12, No. 5, pp. 949-959, 1969.
7. Dinnis, S.C.R. and Walker, J.D.A., "Numerical Solutions for Time-Dependent Flow Past an Impulsively Started Sphere", *The Physics of Fluids*, Vol. 15, No. 4, pp. 517-525, 1972.
8. Li, R. and Boulos, M., "Modeling of Unsteady Flow Around Accelerating Sphere at Moderate Reynolds Numbers", *Canadian Journal of Chemical Engineering*, Vol. 71, No. 6, pp. 837-843, 1993.

9. Kim, I., Elghobashi, S. and Sirignano, W.A., "On the Equation for Spherical-Partical Motion: Effect of Reynolds and Acceleration Numbers", *Journal of Fluid Mechanics*, Vol. 367, pp.221-253, 1998.
10. El-Shaarawi, M.A.I. and Al-Jamal, K., "Forced Convection About a Rotating Sphere", *Applied Energy*, Vol. 43, No.4, pp. 221-238, 1992.
11. Abramzon, B. and Elata, C., "Heat Transfer from a Single Sphere in Stokes Flow", *International Journal of Heat and Mass Transfer*, Vol. 27, No. 5, pp. 687-695, 1984.
12. Feng, Z. and Michaelides, E.E., "Unsteady Heat Transfer From a Sphere at Small Peclet Numbers", *Journal of Fluids Engineering, Transactions of the ASME*, Vol. 118, No. 1, pp. 96-102, 1996.
13. Michaelides, E.E. and Feng, Z., "Heat transfer from a rigid sphere in a nonuniform flow and temperature field", *Int. J. Heat and Mass Transfer*, Vol. 37, No. 14, pp. 2069-2076, 1994.
14. Michaelides, E.E. and Feng, Z., "Transient Heat Transfer From a Particle With Arbitrary Shape and Motion", *Journal of Heat Transfer, Transactions of the ASME*, Vol. 120, No. 3, pp. 674-681, 1998.
15. Ozturk, A. and Ece M.C., "Unsteady Forced Convection Heat Transfer From A Translating and Spinning Body", *Journal of Energy Resources Technology, Transactions of the ASME*, Vol. 117, No. 4, pp. 318-323, 1995.
16. Mansoorzadeh, S., Pain, C.C., De Oliveira, C.R.E. and Goddard, A.J.H., "Finite Element Simulations of Incompressible Flow Past a Heated/Cooled Sphere", *Int. J. Numer. Meth. Fluids*, Vol. 28, No. 6, pp.903-915, 1998.
17. Takhar, H.S., Chamkha, G. and Nath, G., "Unsteady Laminar MHD Flow and Heat Transfer in the Stagnation Region of an Impulsively Spinning and Translating Sphere in the Presence of Buoyancy Forces", *Heat and Mass Transfer*, Vol. 37, No. 4-5, pp.397-402, 2001.
18. Antar, M.A., "Analysis of Fluid Flow and Heat Transfer Around and Inside a Liquid Sphere", *Ph.D. Thesis Mechanical Engineering Department, King Fahd University of Petroleum & Minerals, Dhahran, Saudi Arabia*, 1996.

19. El-Shaarawi, M.I.A., "Derivation of Boundary for Cases With Curved Boundaries", *Int. J. Engineering Fluid Mechanics*, Vol. 3, No. 2, pp 113-118, 1990.
20. Milne-Thomson, L.M., "Theoretical Hydrodynamics", fifth ed., Macmillan and Co., London, 1968.
21. El-Bedeawi, S.A., "The Boundary Layer Flow on a Rotating Body", *Ph.D. Thesis Mechanical Engineering Department, Al-Azhar University, Cairo, Egypt*, 1985.

APPENDIX A

ORDER OF MAGNITUDE ANALYSIS FOR THE GOVERNING EQUATIONS

$$\begin{aligned}
 \text{Re} \gg 1 & \quad , \quad \delta \ll 1 \\
 U = \frac{u}{U_\infty} \approx O(1) & \quad , \quad W = \frac{w}{U_\infty} \approx O(\delta) \\
 Z = \frac{z}{U_\infty} \approx O(\delta) & \quad , \quad X = \frac{2x}{a \text{Re}} \approx O\left(\frac{1}{\text{Re}}\right) \\
 \partial U \approx O(1) & \quad , \quad \partial W \approx O(\delta) \\
 \partial Z \approx O(\delta) & \quad , \quad \partial X \approx O\left(\frac{1}{\text{Re}}\right) \\
 \partial^2 U \approx O(1) & \quad , \quad \partial^2 W \approx O(\delta^2) \\
 \partial^2 Z \approx O(\delta^2) & \quad , \quad \partial^2 X \approx O\left(\frac{1}{\text{Re}^2}\right) \\
 t = \frac{\nu t^*}{a^2} \approx O(1) & \quad , \quad \partial t \approx O(1)
 \end{aligned}$$

A.1 Order of Magnitude Analysis for the Continuity Equation

$$\frac{\partial U}{\partial X} + \frac{\text{Re}}{2} \frac{\partial W}{\partial Z} + \text{Re} \frac{W}{(1+Z)} + \frac{\text{Re}}{2} U \frac{\text{Cot}\theta}{(1+Z)} = 0$$

$$\frac{1}{1/\text{Re}} \quad \text{Re} \left(\frac{\delta}{\delta}\right) \quad \text{Re} \left(\frac{\delta}{1}\right) \quad \text{Re} \left(\frac{1}{1}\right)$$

The third term in this equation has a lower magnitude compared to other terms and can be safely dropped. However, this term will be retained in the equation since it would lead to a simpler solution algorithm for the continuity equations described in Chapter 3.

A.2 Order of Magnitude Analysis for the Meridional Momentum

Equation

$$\begin{aligned} \frac{2}{\text{Re}} \frac{\partial U}{\partial t} + \frac{2}{\text{Re}} U \frac{\partial U}{\partial X} + W \frac{\partial U}{\partial Z} + \frac{UW}{(1+Z)} = -\frac{2}{\text{Re}} \frac{dP}{dX} + \frac{2}{\text{Re}(1+Z)} \frac{\partial^2}{\partial Z^2} (1+Z)U \\ \frac{1}{\text{Re}} \left(\frac{1}{\delta^2}\right) \frac{1}{\text{Re}} (1) \left(\frac{1}{1/\text{Re}}\right) \delta \left(\frac{1}{\delta}\right) \frac{(1)(\delta)}{1} \frac{1}{\text{Re}} \left(\frac{1}{1/\text{Re}}\right) \frac{1}{\text{Re}} \frac{1}{(1)} \frac{1}{\delta^2} (1)(1) \\ + \frac{8}{\text{Re}^3} \frac{\partial^2 U}{\partial X^2} + \frac{4 \cot \theta}{(1+Z) \text{Re}^2} \frac{\partial U}{\partial X} + \frac{8}{(1+Z) \text{Re}^2} \frac{\partial W}{\partial X} - \frac{2U}{(1+Z) \text{Re} \sin^2 \theta} \\ \frac{1}{\text{Re}^3} \left(\frac{1}{1/\text{Re}^2}\right) \frac{1}{(1) \text{Re}^2} \left(\frac{1}{1/\text{Re}}\right) \frac{1}{(1) \text{Re}^2} \left(\frac{\delta}{1/\text{Re}}\right) \frac{1}{(1) \text{Re}} \end{aligned}$$

It is obvious that: $O(\text{Re} \delta^2) \approx 1$ or $\text{Re} \approx O\left(\frac{1}{\delta^2}\right)$

$$O(P) \approx 1$$

Terms of order δ and more can be safely dropped and the meridional momentum equation becomes:

$$\frac{2}{\text{Re}} \frac{\partial U}{\partial t} + \frac{2}{\text{Re}} U \frac{\partial U}{\partial X} + W \frac{\partial U}{\partial Z} = -\frac{2}{\text{Re}} \frac{dP}{dX} + \frac{2}{\text{Re}(1+Z)} \frac{\partial^2}{\partial Z^2} (1+Z)U$$

The last term in the equation can be further simplified as follows;

$$\begin{aligned}
\frac{2}{\text{Re}(1+Z)} \frac{\partial^2}{\partial Z^2} (1+Z)U &= \frac{2}{\text{Re}(1+Z)} \frac{\partial}{\partial Z} \left[\frac{\partial}{\partial Z} (1+Z)U \right] \\
&= \frac{2}{\text{Re}(1+Z)} \frac{\partial}{\partial Z} \left[(1+Z) \frac{\partial U}{\partial Z} + U \right] \\
&= \frac{2}{\text{Re}(1+Z)} \left[(1+Z) \frac{\partial^2 U}{\partial Z^2} + \frac{\partial U}{\partial Z} + \frac{\partial U}{\partial Z} \right]
\end{aligned}$$

or
$$\frac{2}{\text{Re}(1+Z)} \frac{\partial^2}{\partial Z^2} (1+Z)U = \frac{2}{\text{Re}} \frac{\partial^2 U}{\partial Z^2} + \frac{4}{\text{Re}} (1+Z) \frac{\partial U}{\partial Z}$$

$$\frac{1}{\text{Re}} \left(\frac{1}{\delta^2} \right) \quad \frac{1}{\text{Re}} (1) \left(\frac{1}{\delta} \right)$$

The last term is of order δ and can be safely dropped. Hence the meridional momentum equation becomes;

$$\frac{2}{\text{Re}} \frac{\partial U}{\partial t} + \frac{2}{\text{Re}} U \frac{\partial U}{\partial X} + W \frac{\partial U}{\partial Z} = -\frac{2}{\text{Re}} \frac{dP}{dX} + \frac{2}{\text{Re}} \frac{\partial^2 U}{\partial Z^2}$$

At the edge of the boundary layer, meridional velocity component is U^* which is the potential flow around a sphere and it is a function of X only. Substituting in the momentum equation leads to;

$$\frac{2}{\text{Re}} \frac{\partial U^*}{\partial t} + \frac{2}{\text{Re}} U^* \frac{\partial U^*}{\partial X} = -\frac{2}{\text{Re}} \frac{dP}{dX}$$

The potential flow component U^* does not change with time and this led to further simplification of the above equation;

$$\frac{2}{\text{Re}} U^* \frac{\partial U^*}{\partial X} = -\frac{2}{\text{Re}} \frac{dP}{dX}$$

The meridional momentum equation becomes;

$$\frac{2}{\text{Re}} \frac{\partial U}{\partial t} + \frac{2}{\text{Re}} U \frac{\partial U}{\partial X} + W \frac{\partial U}{\partial Z} = \frac{2}{\text{Re}} U^* \frac{\partial U^*}{\partial X} + \frac{2}{\text{Re}} \frac{\partial^2 U}{\partial Z^2}$$

Multiplying the whole equation with (Re/2), the final form of meridional momentum equation becomes;

$$\frac{\partial U}{\partial t} + U \frac{\partial U}{\partial X} + \frac{\text{Re} W}{2} \frac{\partial U}{\partial Z} = U^* \frac{\partial U^*}{\partial X} + \frac{\partial^2 U}{\partial Z^2}$$

A.3 Order of Magnitude Analysis for the Radial Momentum Equation

$$\frac{2}{\text{Re}} \frac{\partial W}{\partial t} + \frac{2}{\text{Re}} U \frac{\partial W}{\partial X} + W \frac{\partial W}{\partial Z} - \frac{U^2}{(1+Z)} = -\frac{1}{2} \frac{dP}{dZ} + \frac{2}{\text{Re}(1+Z)} \frac{\partial^2}{\partial Z^2} (1+Z)W$$

$$\frac{1}{\text{Re}} \left(\frac{\delta}{\delta^2}\right) \quad \frac{1}{\text{Re}} (1) \left(\frac{\delta}{1/\text{Re}}\right) \quad \delta \left(\frac{\delta}{\delta}\right) \quad \frac{1}{1} \quad \left(\frac{P}{\delta}\right) \quad \frac{1}{\text{Re}} \frac{1}{(1)} \frac{1}{\delta^2} (1)(\delta)$$

$$+ \frac{8}{\text{Re}^3} \frac{\partial^2 W}{\partial X^2} + \frac{4 \cot \theta}{(1+Z) \text{Re}^2} \frac{\partial W}{\partial X} - \frac{8}{(1+Z) \text{Re}^2} \frac{\partial U}{\partial X} - \frac{4W}{(1+Z)^2 \text{Re}^2} - \frac{4U \cot \theta}{\text{Re}(1+Z)^2}$$

$$\frac{1}{\text{Re}^3} \left(\frac{\delta^2}{1/\text{Re}^2}\right) \quad \frac{1}{(1) \text{Re}^2} \left(\frac{\delta}{1/\text{Re}}\right) \quad \frac{1}{(1) \text{Re}^2} \left(\frac{1}{1/\text{Re}}\right) \quad \frac{\delta}{(1) \text{Re}^2} \quad \frac{1}{\text{Re}}$$

From the above equation, we get $1=P/\delta$ which indicates that the variation of pressure in the boundary layer is proportional to δ and it can be neglected. Therefore, dropping the terms of order δ and higher order leads to safely dropping the whole equation.

VITAE

Name: Fayez Hasen Mohammed Al-Ghamdi

Date of Birth: 29th April, 1969

Marital Status: Married (+ 4 children)

Education: B.Sc. in Mechanical Engineering, KFUPM, with degree of honor, January, 1993.

Joined KFUPM as a Master student, September, 2000.

M.Sc. in Mechanical Engineering, KFUPM, March, 2004.